

Electrons and magnetic fields in the lunar plasma wake

J. S. Halekas, S. D. Bale, D. L. Mitchell, and R. P. Lin

Space Sciences Laboratory, University of California, Berkeley, California, USA

Received 22 December 2004; revised 30 March 2005; accepted 9 May 2005; published 22 July 2005.

[1] Earth's Moon, lacking both a global magnetic field and any significant atmosphere, presents an ideal location to study plasma flow past a solar system body in one of its simplest incarnations. Despite its relative simplicity, however, the lunar wake interaction displays a rich array of physics, with both fluid and kinetic aspects. We present a new study of the lunar wake, using measurements from Lunar Prospector (LP) to determine the magnetic field, electron density and temperature, and electrostatic potential. We use these data and Wind key parameter data to characterize the wake near the Moon. At 85–115 km above the Moon we observe a “classical” wake signature, with enhanced magnetic fields in the central wake and reduced fields near the boundary. The magnetic signature at these altitudes responds clearly to changes in solar wind parameters, while that at 20–45 km depends mainly on crustal fields. We also observe an ambipolar potential drop across the wake boundary (resulting in central wake potentials of about -300 V relative to the solar wind) and greatly reduced electron density and increased electron temperature in the wake. The wake morphology, in terms of both electron parameters and magnetic fields, is well described by self-similar solutions for plasma expansion into a void and the resulting diamagnetic current system, but only if Kappa functions are used to describe the solar wind electron distributions.

Citation: Halekas, J. S., S. D. Bale, D. L. Mitchell, and R. P. Lin (2005), Electrons and magnetic fields in the lunar plasma wake, *J. Geophys. Res.*, 110, A07222, doi:10.1029/2004JA010991.

1. Introduction

[2] The Moon has a very minimal atmosphere/exosphere and no global magnetic field, though regions of remanent crustal magnetization ranging in size from a few km or less to hundreds of km cover much of the lunar surface, with magnetic fields at 20–30 km altitude as high as 50 nT, and surface fields as high as several hundred or even a few thousand nT [Hood *et al.*, 2001; Halekas *et al.*, 2001]. When the Moon lies outside of the Earth's magnetosheath ($\sim 75\%$ of the time), it is exposed to the solar wind. Solar wind magnetic fields pass through the relatively nonconductive lunar surface essentially unimpeded, with only a slight inductive interaction with the more electrically conducting interior [Sonett, 1982]. To first order, solar wind plasma impacts the surface directly and is absorbed [Goldstein, 1974], leading to the formation of a plasma cavity and wake structure behind the lunar obstacle.

[3] The Explorer 35 spacecraft and the Apollo 15 and 16 subsatellites [Ness, 1972; Schubert and Lichtenstein, 1974, and references therein] provided the first observations of the lunar plasma wake. Explorer 35 surveyed the wake at distances of 1000–10,000 km from the surface of the Moon, while the Apollo subsatellites provided limited coverage in a region ~ 100 –160 km above the lunar surface. More recently, particle and magnetic field data from the Wind spacecraft revealed a wake signature at $\sim 11,000$ km

($6.5 R_L$) downstream from the Moon [Bosqued *et al.*, 1996; Ogilvie *et al.*, 1996; Owen *et al.*, 1996], and data from NOZOMI [Futaana *et al.*, 2001] and GEOTAIL [Nakagawa *et al.*, 2003] also provided indirect evidence of electric fields related to the lunar wake.

[4] The lunar wake, a region of greatly reduced plasma density (due to the absorption of solar wind plasma by the lunar obstacle), typically has somewhat stronger magnetic fields than those in the ambient solar wind, while an expansion region with reduced magnetic fields surrounds the central wake [e.g., Ness *et al.*, 1968; Colburn *et al.*, 1967, 1971]. Colburn *et al.* [1967] successfully explained these observations in terms of diamagnetic current systems on the surface of the wake boundary (set up by the pressure gradient across the boundary) that amplify the magnetic field inside the wake and decrease it outside. The main magnetic field perturbations have also been successfully described in a fluid pressure balance picture in terms of plasma expansion and recompression [Whang, 1968a, 1968b; Johnson and Midgeley, 1968; Michel, 1968]. Outside of the expansion region, however, sharply peaked magnetic enhancements known as “limb shocks” or “limb compressions” (for convenience, we will hereafter refer to these magnetic field enhancements as limb shocks, though they may not in fact be shocks at all) are occasionally found [Ness *et al.*, 1968; Colburn *et al.*, 1971; Russell and Lichtenstein, 1975; Lin *et al.*, 1998] that cannot be explained in terms of either current systems or pressure balance, unless a source of backpressure is available to deflect and compress or shock the solar wind. Researchers have proposed a variety of sources for this

backpressure, including a tenuous lunar atmosphere [Siscoe and Mukherjee, 1972], induced magnetic fields in electrically isolated “conducting islands” [Hollweg, 1970], and remanent crustal magnetic fields [Sonett and Mihalov, 1972]. Observations have established that the enhancements preferentially occur when regions with strong crustal magnetic fields lie near the limb [Russell and Lichtenstein, 1975; Sonett and Mihalov, 1972], lending support to the latter hypothesis. Statistical studies using Explorer 35 data indicate that the wake magnetic field structure varies with solar wind β and Kp values, as well as other parameters such as the ion thermal speed and solar wind magnetic field orientation [Ogilvie and Ness, 1969; Colburn et al., 1971; Whang and Ness, 1972]. However, a clear understanding of how the structure of the lunar wake depends on various solar wind parameters has not yet emerged.

[5] The lunar wake also has a characteristic particle signature. Data from the Wind spacecraft showed the presence of ion beams refilling the wake from the sides [Ogilvie et al., 1996], which have since been found to have large temperature anisotropies [Clack et al., 2004]. The ion beams were used to infer the presence of an ambipolar potential drop of several hundred volts across the wake boundary. Observations by the NOZOMI and GEOTAIL spacecraft of counterstreaming electrons and waves in the vicinity of the lunar wake probably also reveal the effects of this potential [Futaana et al., 2001; Nakagawa et al., 2003], which appears to be a consequence of the charge separation caused by electrons attempting to refill the wake ahead of the slower ions [Samir et al., 1983]. Meanwhile, recent measurements from Lunar Prospector show the presence of a potential drop of ~ 50 volts over a distance of ~ 1 km above the lunar surface inside the wake region [Halekas et al., 2002, 2003]. This near-surface potential drop is likely unrelated to the potential drop across the wake boundary, since the wake potential appears to extend over a considerable distance, while the surface potential is confined to a thin sheath above the surface. Previous investigations, using data from one or several orbits, have not been capable of determining the global structure of the wake potential, though simulations and theoretical work have begun to attack this problem [Farrell et al., 1998; Birch and Chapman, 2001; Borisov and Mall, 2000, 2002]. Furthermore, little work has addressed how the wake potential and other charged particle properties depend on solar wind parameters.

[6] In this work, we exploit the large volume of Lunar Prospector (LP) data, along with the presence of Wind as an independent monitor of ambient solar wind conditions, to investigate the 3-D magnetic field and charged particle structure of the lunar wake near the Moon, and to determine how this structure depends upon solar wind parameters. We focus on the basic interaction between the solar wind and the Moon, and the physics of the plasma wake that is created as a result of this interaction. While the limb shocks represent one aspect of this interaction and will therefore be briefly discussed, research on these features is ongoing and is not the focus of this work.

2. Data Analysis

[7] For any given LP orbit, a large number of variables can affect the lunar wake structure and therefore the

magnetic fields and electron distributions we observe. These may include any and all solar wind parameters (especially the solar wind velocity and magnetic field orientation), the inclination of the orbit with respect to the solar wind, the geographic region of the Moon (and therefore the crustal magnetic fields) below LP, the orbital altitude, and possibly other parameters. However, we have the advantage of starting with a database of more than 6000 near-circular polar LP orbits, with orbits at altitudes of ~ 100 km from the first year of the mission (1998) and at 20–50 km from the last six months (in 1999). Using this large volume of data, we can map out magnetic fields and electron parameters with respect to geographic position on the lunar surface, orientation with respect to the solar wind, and altitude, in a shell around the Moon. Furthermore, we can sort data by any desired solar wind parameter. This allows us, at least to some degree, to determine the effects of all the variables that may affect the wake structure.

2.1. Data Sources

[8] Our primary data come from the LP Magnetometer/Electron Reflectometer (MAG/ER) experiment. The MAG/ER, consisting of a triaxial fluxgate magnetometer and a top hat electrostatic analyzer, generates full 3-D electron distribution functions (at energies of ~ 40 eV to 20 keV) with 80 s time resolution, along with pitch angle-sorted data for selected energies at much higher time resolutions (up to 2.5 s), and three-axis magnetic field measurements at 9 Hz. We primarily use the full 3-D distribution data to generate energy spectra and determine relevant electron parameters. Since we are not concerned in this work with waves (though the interaction of the solar wind with the Moon generates waves whose study may prove very interesting), we time-average the magnetic field data to 20 s resolution to allow us to deal with a manageable volume of data for each orbit. Though we are necessarily limited by the lack of ion data, we can still derive or infer many relevant parameters from MAG/ER data, allowing us to well characterize the relevant physics. Furthermore, the rapidly precessing polar orbit of LP ensures good coverage over the entire surface of the Moon for a full range of orbital inclinations.

[9] In addition, we use data from the Wind spacecraft to monitor the ambient solar wind conditions. In particular, we use key parameter data (1-min resolution) from the Wind Solar Wind Experiment (SWE) [Ogilvie et al., 1995] to determine the solar wind proton velocity, density, and temperature, and from the Wind Magnetic Field Investigation (MFI) [Lepping et al., 1995] to determine the solar wind magnetic field. By time shifting these data appropriately, given the spacecraft separation and the solar wind velocity (again from SWE key parameters), we can use the Wind and LP data sets in concert [Lin et al., 1998].

[10] Finally, we use the primary data products from the MAG/ER; namely, the maps of crustal magnetic field magnitude and direction produced independently from magnetic field measurements at orbital altitude [Hood et al., 2001] and electron reflectometry [Halekas et al., 2001], to characterize the unperturbed lunar crustal magnetic topology.

2.2. Data Selection

[11] The initial data selection proceeds essentially “by hand.” For each LP orbit, we first determine whether the

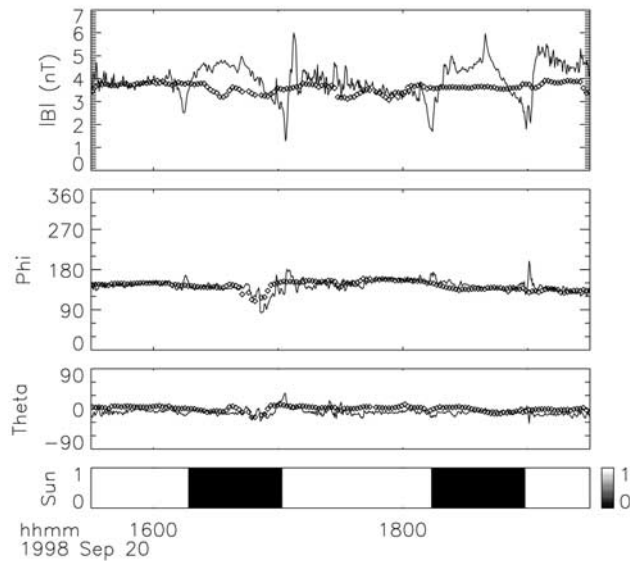


Figure 1. LP magnetic field and direction angles in selenographic solar ecliptic (SSE) coordinates (solid lines) on 20 September 1998 and corresponding Wind measurements, appropriately shifted in time to take into account the separation between the two spacecraft and the solar wind velocity (diamonds). The solid bar at the bottom shows when LP is in sunlight and shadow.

Moon is outside of the influence of the Earth’s magnetic field by checking the position of the Moon with respect to the Earth and the Sun, and double-checking by searching for magnetic field turbulence expected in the magnetosheath and foreshock regions, and discard orbits in regions influenced by the Earth’s magnetic field. We then use the solar wind velocity from Wind key parameters, and the positions of the Wind and LP spacecraft, to time-shift the Wind data appropriately to account for the solar wind travel time between the two spacecraft. Magnetic field data for one LP orbit are shown in Figure 1, along with time-shifted Wind magnetic field data. For this orbit, the magnetic field magnitude and direction observed at the two spacecraft correspond closely, except near the limb and in the solar wind wake, where large perturbations to the magnetic field magnitude are clearly seen in the LP data, along with small rotations. We discard orbits where, unlike in this case, the unperturbed magnetic field direction and/or inclination observed at the two spacecraft do not correspond. A variety of phenomena may lead to such a mismatch, including but not limited to, structure in the solar wind between Wind and LP, the Wind spacecraft traversing a region affected by the Earth’s magnetic field (either the magnetosphere and/or magnetosheath itself, or the foreshock region), or LP in the magnetosheath or foreshock (but not caught by the previous selection step). Whatever the cause, we discard all orbits where the time-shifted magnetic field data do not agree. Using this procedure, we selected 3813 orbits of usable data, most lying in two shells around the Moon, at altitudes of 85–115 km (the initial LP mapping orbit) and 20–45 km (the lower-altitude extended mission).

[12] For each orbit that passed our selection criteria, we saved the LP magnetic field, along with the LP position, and

the average and standard deviation of the solar wind magnetic field and the solar wind proton density, velocity, and temperature. Average solar wind parameters are shown for the selected orbits in Table 1. We then proceeded to calculate the relevant electron parameters, as described below.

2.3. Calculating Electron Parameters

[13] Some care is necessary when using and interpreting the electron distributions from the LP ER. First of all, only the electrons going toward the Moon should be used in the analysis, since the upward going electron distributions on magnetic field lines connected to the lunar surface may depend strongly on the properties of the surface at the foot point of the field line, including remanent crustal magnetization and photoemission and secondary emission characteristics [Halekas *et al.*, 2001, 2002]. Furthermore, at most times, the lowest energy measured by the ER is ~ 40 eV, which does not allow for accurate direct integration of the energy distribution to determine moments such as density and temperature. However, we have found it possible to fit the energy distribution to a Kappa function and thereby derive an approximate electron density and temperature [Halekas *et al.*, 2002]. This can only be considered an approximation, since it does not take into account any change in the shape of the distribution function below ~ 40 eV due to, for instance, a secondary low-energy electron population. Indeed, we find that our estimates of solar wind electron density from LP are low compared to the estimates of solar wind proton density from Wind key parameters (see Table 1), even when taking into account the fact that we only use half the distribution (the density value in Table 1 is already doubled to account for this). This discrepancy may be due in some way to the proximity of the Moon to LP and/or instrument calibration issues, or it may be completely a result of the different methods used to calculate the two sets of moments (Wind moments are calculated by direct integration). However, assuming that distributions are well fit by a single Kappa function (true in general for the energies we can observe), this fit provides at least an approximation to the true electron density and temperature. Examples of successful fits both inside and outside the wake are shown in Figure 2. Electron spectra that are not well fit by Kappa functions (as determined by a chi-squared goodness-of-fit parameter) can be discarded.

[14] At many times, the energy spectrum inside the wake, for at least a range of energies, is identical to the spectrum outside, other than a shift in energy. Figure 2 shows an example of such an orbit. In this case, our interpretation is that the electrons in this energy range have essentially free access to the wake, and that the shift in energy can be

Table 1. Average Solar Wind Parameters

Parameter	Value
Proton density (Wind)	7.88 cm^{-3}
Proton temperature (Wind)	8.09 eV
Solar wind velocity (Wind)	410 km/s
Magnetic field (Wind)	6.86 nT
Alfvén speed (Wind)	53 km/s
Electron Kappa parameter (LP)	4.5
Electron Kappa density (LP)	3.5 cm^{-3}
Electron Kappa temperature (LP)	20 eV
Sound speed (LP)	44 km/s

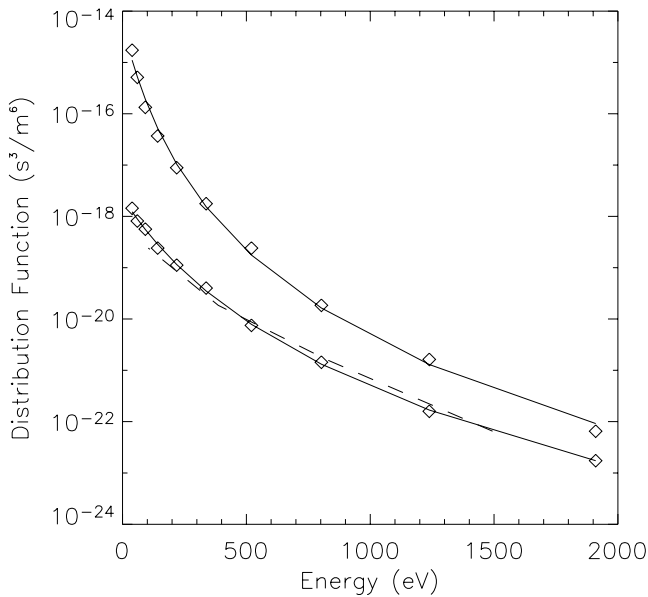


Figure 2. LP electron data for electrons traveling toward the Moon (diamonds), upstream of the Moon (17:35 UT) and inside the wake (16:45 UT) on one orbit on 20 September 1998. Solid lines show Kappa function fits (fitted upstream and wake densities are 0.86 and 0.0016 cm^{-3} , temperatures are 33 and 93 eV , and kappa parameters are 5.66 and 5.52). The dashed line shows the upstream distribution function in the energy range of $500\text{--}2000 \text{ eV}$, shifted by 416 V .

interpreted as an electrostatic potential difference between the wake and the solar wind. For this interpretation to remain valid, of course, solar wind conditions (and thus the solar wind electron distribution) must also remain relatively steady during the orbit in question. In practice, to find orbits where a potential difference can be successfully derived, we choose a reference spectrum in the solar wind for each LP orbit. We then select data from the reference spectrum for energies of $500\text{--}2000 \text{ eV}$ (high enough energy that all electrons in question should be able to make it all the way into the wake, but low enough energy to ensure good counting statistics). Then, for each energy in each sample electron spectrum in the given orbit, we compare to the reference spectrum to determine at what reference energy the sample distribution function is equal to the reference distribution function. By subtracting the sample energies from the corresponding reference energies we derive a set of energy shifts for each sample spectrum. We average these energy shifts to determine an average sample energy shift with respect to the reference spectrum. We then calculate the standard deviation of the energy shifts. If this number is relatively small, then the energy spectra are consistent with a single energy shift as the electrons pass through an electrostatic potential drop. If the standard deviation is high, on the other hand, it is clear that, for whatever reason (probably particle access issues), we cannot interpret the data in this way. In the case shown in Figure 2, the standard deviation is only a few tens of eV (as we should expect, since the Kappa function fits are quite good, and the derived kappa parameters are nearly the same since a shifted Kappa function has the same kappa param-

eter), and the interpretation of a single energy shift appears valid. We are unfortunately unable to correct for the charging of the spacecraft itself, and so the potential we derive is actually the spacecraft potential, which will likely be more negative than the plasma potential in shadow. However, previous experience and basic calculations show that the spacecraft potential is unlikely to be more than 100 V negative with respect to the plasma [Halekas et al., 2002]. In any case, the potential derived in shadow should be considered a lower limit on the plasma potential.

[15] In practice, we choose two reference spectra per orbit, one at the beginning of the orbit and one at the end. We calculate potential differences for each reference spectrum, and then splice the two by picking a joining point such that the average standard deviation in the energy shifts is minimized. Therefore, if there is a change in the solar wind conditions midway through the orbit, we can still derive potential differences for the whole orbit. All of this calculation proceeds automatically, using IDL computer programs.

2.4. Normalizing Data

[16] The ranges of magnetic field magnitudes and electron densities and temperatures observed in the solar wind are large. These large variations in our baseline can make it difficult to detect small relative variations. Therefore we generally normalize all variables. We normalize the magnetic field magnitude by dividing by the average solar wind magnetic field magnitude for the given orbit, as determined from Wind MFI data. One may argue that this normalization could be somewhat misleading, since magnetic fields can vary in inclination as well as magnitude; however, in our experience the variations in inclination between the LP and the Wind magnetic field data are minimal when compared to the perturbations in magnitude seen in the LP data. We similarly normalize electron densities and temperatures by the average density or temperature derived for the given orbit from LP data above the sunlit hemisphere of the Moon, which is valid because the electron density and temperature vary relatively little in the sunlit hemisphere for a given orbit, with very large variations present in the shadowed hemisphere.

[17] Finally, since the zero level of the electrostatic potential is completely arbitrary, we must find some way to appropriately compare potential data from different orbits. We accomplish this by setting the electrostatic potential equal to zero at the limb. Each orbit crosses the limb exactly twice, so this normalization can be meaningfully applied. The only drawback of this normalization comes if there is a significant variation in potential with altitude at the limb. However, we felt that this normalization represented the best compromise. Setting the potential equal to zero at most other reasonable points or lines, such as the subsolar point, would not work, since not all orbits would cross that point or line. Setting the average potential of the whole sunlit hemisphere equal to zero would not work either, since we do observe some variations in potential over the sunlit hemisphere.

2.5. Coordinate Systems

[18] Three main coordinate systems are used in this paper, all of which are standard right-handed coordinate systems.

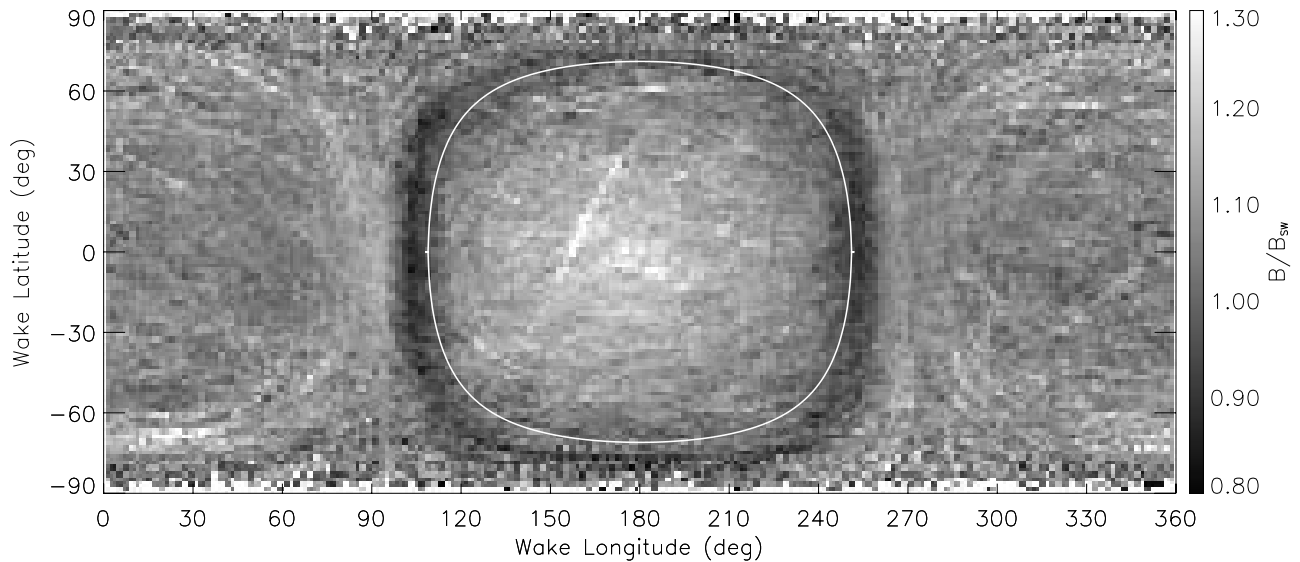


Figure 3. Normalized LP magnetic field measurements from altitudes of 85–115 km, binned by wake longitude and latitude. The white circle shows the solar wind flow terminator. See color version of this figure at back of this issue.

The first steps of the data analysis are carried out in selenocentric solar ecliptic (SSE) coordinates. These coordinates are completely analogous to GSE coordinates, and are defined so that the x axis points toward the Sun and the z axis is normal to the ecliptic plane. We also occasionally use selenographic (SEL) coordinates, which are simply Moon-fixed geographic coordinates. Finally, for most of the analysis presented in this paper, we rotate data into what we call “wake coordinates.” We define these coordinates so that the x axis is antiparallel to the aberrated solar wind velocity (the aberration is calculated using the solar wind velocity from the Wind SWE key parameters and the known orbital parameters of the Moon), and the magnetic field direction is in the x - z plane. In practice, the wake x axis is usually within several degrees of the SSE x axis (since the aberrated solar wind flow is close to the Sun-Moon line), but the z axis is rotated significantly depending on the solar wind magnetic field direction. These wake coordinates allow us to determine the symmetry properties of the wake with respect to the magnetic field direction.

[19] We often select data from within some range of clock angles from the wake x - z plane (quasi-parallel to the magnetic field) or from within some range of clock angles from the wake x - y plane (quasi-perpendicular to the magnetic field). Finally, when we present data in terms of wake longitude and latitude, one can simply remember that the wake axis (antiparallel to the aberrated solar wind velocity) lies at a wake latitude and longitude of 0, and that the magnetic field direction lies at positive wake latitudes and a wake longitude of either 0 or 180 (depending on whether $\vec{B} \bullet \vec{v}$ is negative or positive).

3. Results

[20] In this section we present basic results from the data analysis described in the preceding section, showing the 3-D structure of the lunar plasma wake, as revealed by LP MAG/ER measurements, in terms of both magnetic fields

and electron parameters. We go on to present the results of analyses focusing on the variation of the lunar wake structure with solar wind parameters and the physics of how plasma fills in the wake.

3.1. Basic Results

[21] We show normalized magnetic fields binned by wake longitude and latitude, for high and low orbital altitudes, in Figures 3 and 4. We clearly see the expected wake magnetic signature, consisting of enhanced magnetic fields (B/B_{sw} of 1.1–1.3) inside the wake cavity, and reduced fields (B/B_{sw} of 0.85–1.0) in the surrounding expansion region, in the high-altitude data of Figure 3. The boundary between enhanced and reduced magnetic fields corresponds closely with the solar wind flow terminator (which is not the same as the optical terminator due to solar wind aberration, and is crossed by the spacecraft at different points, depending on the orbital altitude). This alignment corresponds to expectations, since the peak of the diamagnetic current system should lie at the boundary of the solar wind flow, at the peak pressure gradient between the solar wind plasma and the wake cavity. Forward of the expansion region lies a region of slightly enhanced magnetic fields (B/B_{sw} of 1.1–1.2), which are a manifestation of the limb shocks reported by many previous authors [e.g., *Ness et al.*, 1968; *Colburn et al.*, 1971; *Russell and Lichtenstein*, 1975]. On average, the enhancement is not great; however, on individual orbits magnetic fields can be enhanced by factors as high as 3–4 forward of the wake and expansion regions. The variability in the average high-altitude magnetic signature is substantial (on the order of 10–15%), and is fairly constant except in the limb shock regions where it increases somewhat. Despite this variability, the average signature varies smoothly.

[22] In contrast to the data shown in Figure 3, the low-altitude data in Figure 4 are much more disordered. We observe the same basic features, but much less clearly and distinctly, because lunar crustal magnetic fields contribute much more significantly at lower altitudes. We show exactly

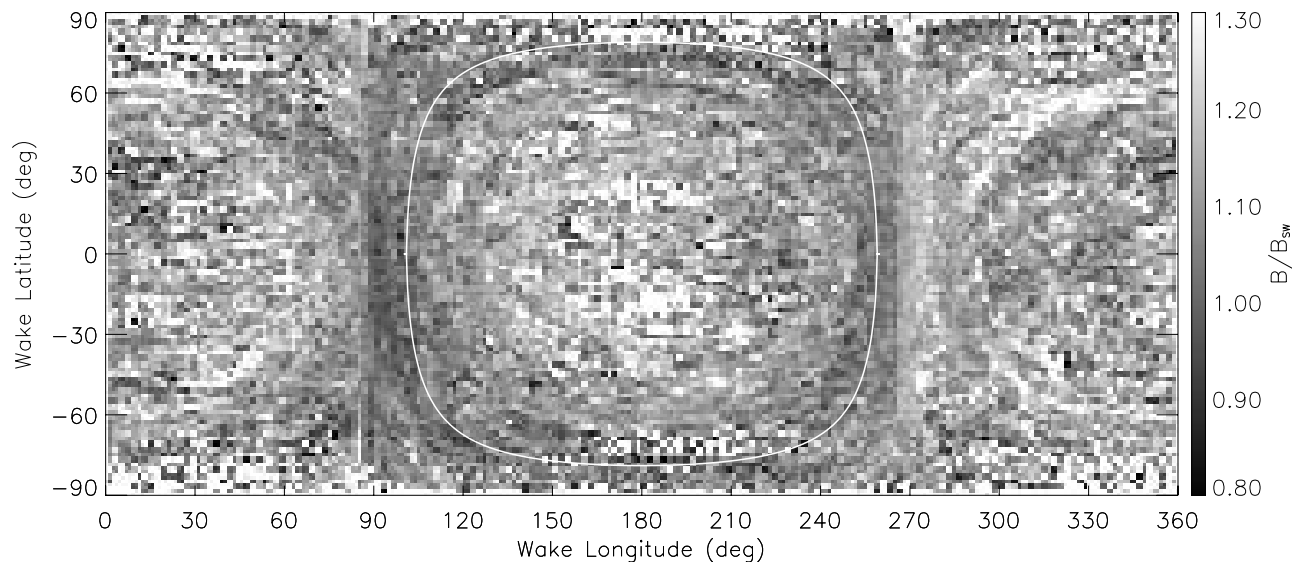


Figure 4. Normalized LP magnetic field measurements from altitudes of 20–45 km, binned by wake longitude and latitude. The white circle shows the solar wind flow terminator. See color version of this figure at back of this issue.

the same low-altitude data in Figure 5, but now rotated into Moon-fixed SEL coordinates. We recognize that this map is dominated by remanent crustal magnetic fields [Halekas *et al.*, 2001; Hood *et al.*, 2001], confirming that the signal due to crustal fields dominates over the perturbation due to the wake interaction at lower altitudes. The average normalized magnetic field, even on the dayside, is somewhat larger than unity. It appears likely that this is also because of the presence of the lunar remanent crustal magnetic fields. Normalized dayside magnetic fields are even larger at low altitudes than at high altitudes, supporting this basic conclusion.

[23] We show normalized electron density and temperature, and electrostatic potential, derived by the means

discussed previously, and binned by wake longitude and latitude, in Figures 6–8. In contrast to magnetic field data, we plot electron data from all altitudes simultaneously. We have found that the variation of the electron parameters over the small range of altitudes covered by LP is minimal compared to the variation with angle from the wake axis. On average, the electron density drops by over two orders of magnitude from the solar wind to the wake cavity, while the electron temperature rises by up to an order of magnitude, and the electrostatic potential drops by several hundred volts. The variability is substantial, on the order of 20–40% for the electron density and temperature (except for the temperature in the central wake, which is even more variable), and on the order of ~ 100 V for the potential.

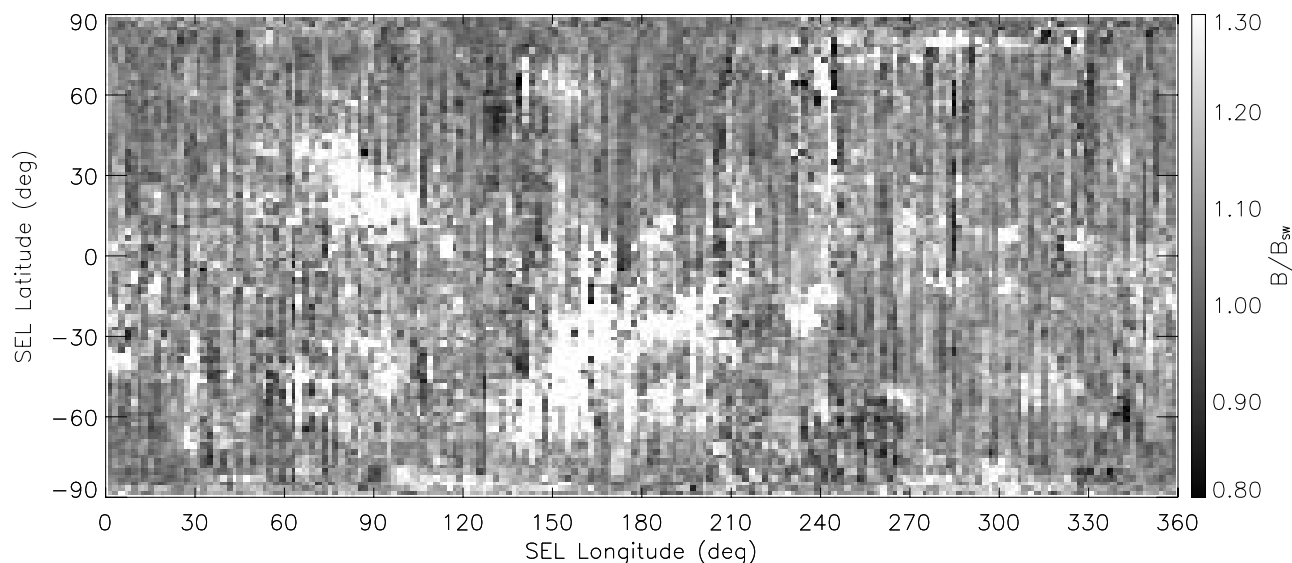


Figure 5. Normalized LP magnetic field measurements from altitudes of 20–45 km, binned by selenographic (SEL) longitude and latitude. See color version of this figure at back of this issue.

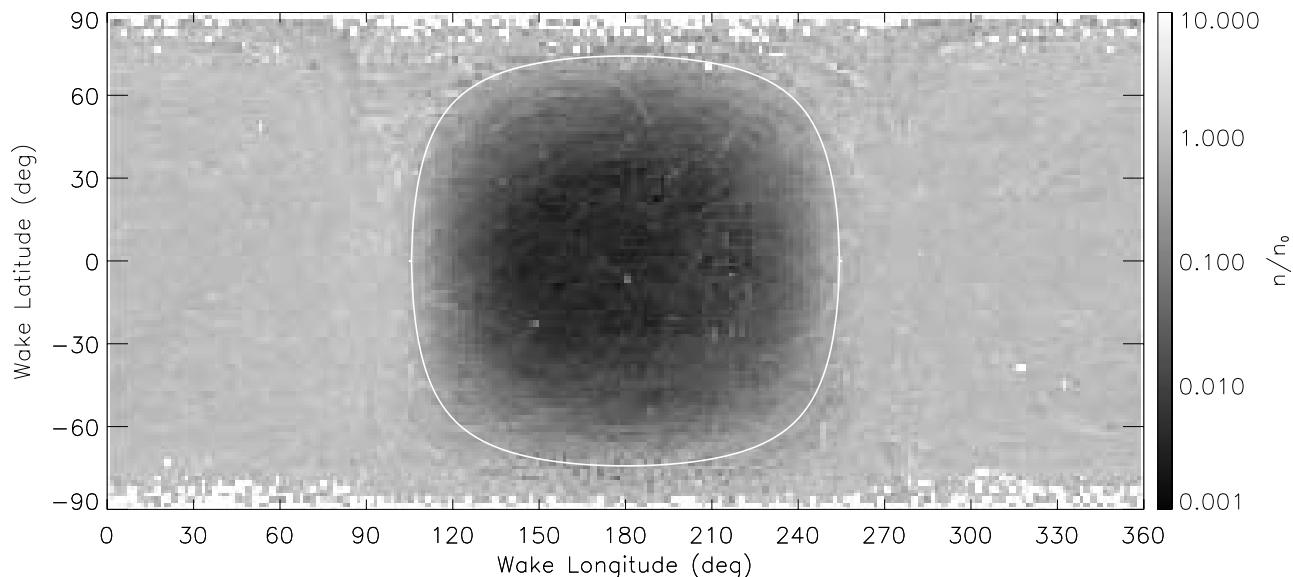


Figure 6. Normalized LP electron density measurements from altitudes of 20–115 km, binned by wake longitude and latitude. The white circle shows the solar wind flow terminator. See color version of this figure at back of this issue.

The electron density drop is very closely correlated with the flow terminator, as expected. We find no increase in electron density correlated with the limb shocks that could be identified as plasma compression (early investigations showed some enhancement in the density, but this was apparently caused by distributions that were not well fit by Kappa functions, and was in any case not correlated with magnetic field enhancements). This stands in contrast to ion observations by *Siscoe et al.* [1969], who found some evidence of plasma compression associated with limb shocks. Meanwhile, the electrostatic potential drop is more gradual, but also correlated with the flow terminator. As

discussed by *Ogilvie et al.* [1996], and explained in detail by *Samir et al.* [1983, and references therein], the potential drop is due to the faster electrons “outrunning” the ions as they attempt to fill in the wake cavity. This leads to charge separation and an ambipolar potential drop. The increase in electron temperature in the wake is more unexpected, but has also been previously observed [*Ogilvie et al.*, 1996; *Halekas et al.*, 2002], and is a natural consequence of the potential drop across the wake boundary and the nature of the solar wind electron distributions. Because solar wind electron distributions are not satisfactorily described by Maxwellians, but instead have high-energy tails that are

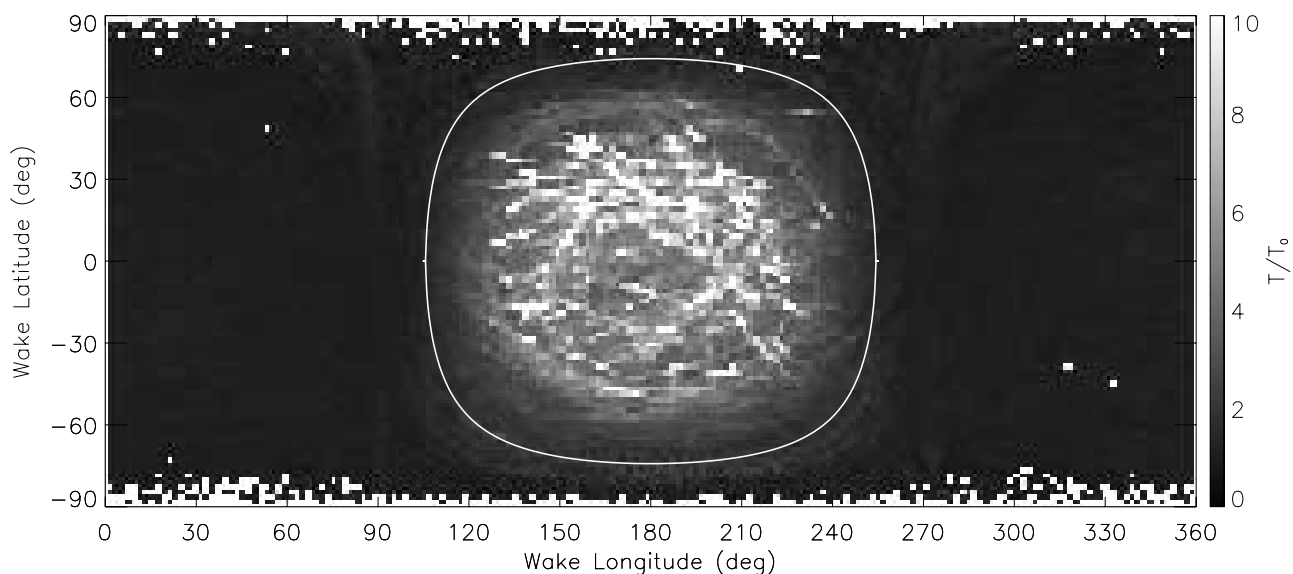


Figure 7. Normalized LP electron temperature measurements from altitudes of 20–115 km, binned by wake longitude and latitude. The white circle shows the solar wind flow terminator. See color version of this figure at back of this issue.

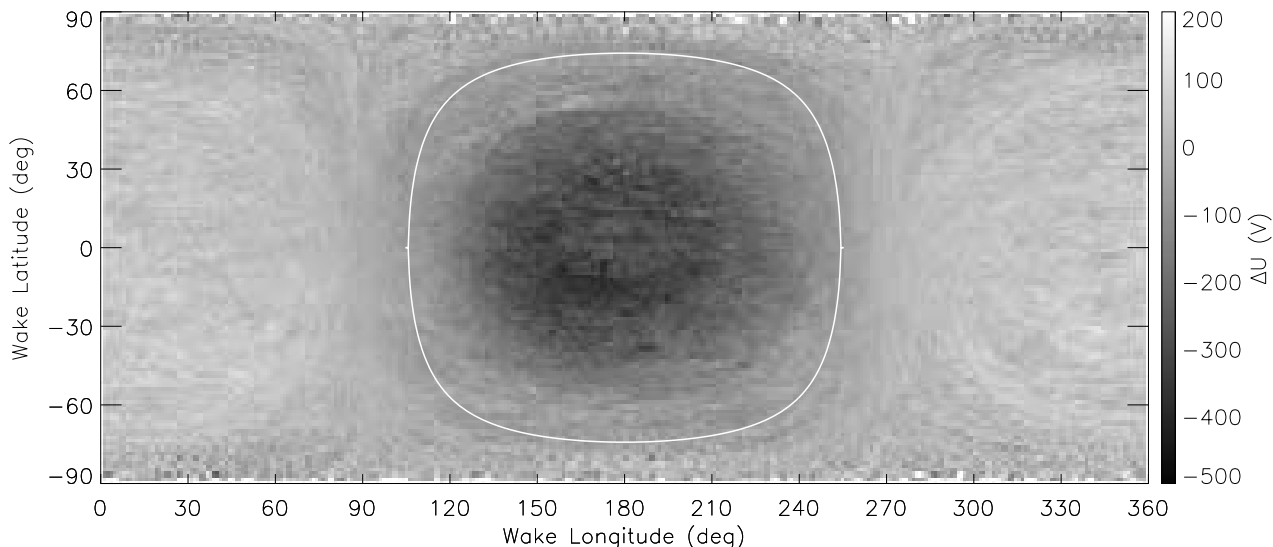


Figure 8. LP electrostatic potential measurements from altitudes of 20–115 km, binned by wake longitude and latitude. The white circle shows the solar wind flow terminator. See color version of this figure at back of this issue.

more aptly described by Kappa functions, filtering a solar wind electron distribution by passing it through an ambipolar potential drop does not result in a wake distribution with the same kinetic temperature; rather, a distribution with a higher temperature results. This process is known as velocity filtration, and has been discussed in detail by Scudder [1992].

[24] The color plates presented so far give a good overview of magnetic field and electron behavior in a shell around the Moon. However, it can be difficult to pick out minor asymmetries and to get a good idea of the magnitude of small perturbations in these plates. We therefore present the same data in a different format in Figures 9–13. In this new format, we bin data by the angle from the wake x axis, since the wake is approximately rotationally symmetric around this axis. To address the presence of small rotational asymmetries, we split the wake into two regions according to the clock angle in a plane perpendicular to the x axis: regions within 45° of the wake x - z plane (quasi-parallel to the magnetic field), and regions within 45° of the wake x - y plane (quasi-perpendicular to the magnetic field).

[25] We find that only the high-altitude magnetic fields show substantial rotational asymmetry around the wake axis. In particular, the magnitude of the magnetic field depression in the expansion region is larger in quasi-perpendicular regions, and limb shocks peak farther back (closer to the flow terminator). The first asymmetry can be understood as follows. The magnetic field depression can be characterized in terms of diamagnetic currents, expressed in terms of the cross product of the magnetic field and the pressure gradient [$\vec{J} = (\vec{B} \times \nabla p)/B^2$]. The pressure gradient points radially inward (perpendicular to the wake axis). Therefore the cross product with the magnetic field is greater, on average, for quasi-perpendicular regions than for quasi-parallel regions (where the magnetic field is on average more radial). Later, when we look at specific solar wind magnetic field orientations, this distinction will become even more apparent. As for the difference in limb

shock location, the cause of this phenomenon, if real, is unknown. For low-altitude magnetic field data, meanwhile, any asymmetries are not readily apparent above the noise level caused by the large contribution from crustal magnetic fields.

[26] Finally, other than a high level of variability for the electron temperature in the central wake, the various electron parameters are smoothly varying and nearly perfectly rotationally symmetric about the wake axis.

3.2. Solar Wind Control

[27] In this section we address the variation of the wake structure with solar wind parameters. We choose two variables to look at in detail: the high-altitude normalized magnetic field and the electrostatic potential. The magnetic field and the electrostatic potential are perhaps the two most fundamental parameters, and we choose only the high-

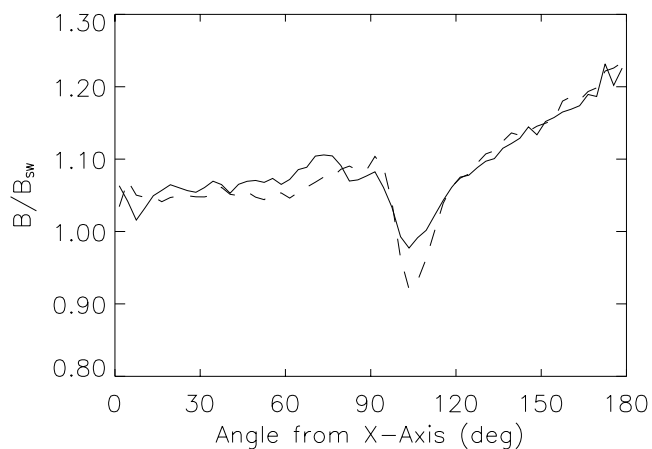


Figure 9. Normalized LP magnetic field measurements from orbital altitudes of 85–115 km, binned by angle from the wake axis, within 45° of the x - z plane (solid line) and within 45° of the x - y plane (dashed line).

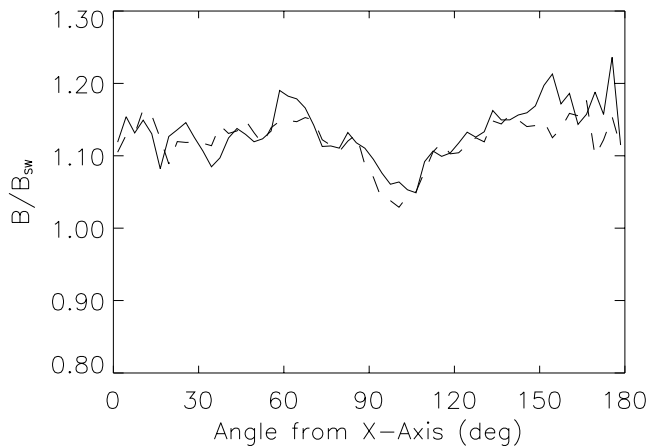


Figure 10. Normalized LP magnetic field measurements from orbital altitudes of 20–45 km, binned by angle from the wake axis, within 45° of the x - z plane (solid line) and within 45° of the x - y plane (dashed line).

altitude magnetic field because the perturbations due to the wake interaction are most clearly seen in these data. We show these data, sorted by a variety of different solar wind parameters, in Figures 14 and 15, in a similar format to that of Figures 9–13. Since we have found that the data are essentially rotationally symmetric around the wake axis, we do not split the wake into regions quasi-parallel and quasi-perpendicular to the magnetic field, except in the second and third panels, where we look at the variation with solar wind magnetic field direction. In those two panels we show data from quasi-parallel and quasi-perpendicular regions of the wake separately.

[28] The relative perturbations in the normalized magnetic field are greater for smaller solar wind magnetic fields, perhaps partly because diamagnetic currents scale inversely in magnitude with the magnetic field. The magnetic field depression in the expansion region is less when the solar wind magnetic field and velocity are perpendicular than when they are parallel in both quasi-parallel and quasi-perpendicular regions of the wake. However, this distinction is much more pronounced in quasi-parallel regions of the wake, as we expect. In quasi-parallel regions, the magnetic fields and pressure gradients are only close to perpendicular (which causes larger diamagnetic currents and therefore larger magnetic perturbations) if the solar wind velocity and magnetic field are parallel. In quasi-perpendicular regions, the magnetic fields and pressure gradients are always close to perpendicular, regardless of solar wind magnetic field orientation. Both the central wake enhancement and the depression in the expansion region are larger for smaller solar wind velocity, probably because, at the (fixed) LP orbital altitude, the magnetic field configuration has had more time to respond to the presence of the diamagnetic cavity when the flow is slower. Very little variation is seen for different ranges of solar wind proton temperatures, though dayside fields appear slightly lower for lower proton temperature. The central wake enhancement is clearly larger for larger proton density, dynamic pressure, and proton β , as expected since to maintain pressure balance this enhancement should scale roughly

with solar wind plasma pressure, which correlates with all of these variables. The dayside fields and the depression in the enhancement region are also slightly larger for larger proton β . These plots show no clear evidence for solar wind control of the limb shocks. This is primarily because the limb shocks are a transient feature only present on a small fraction of the orbits, and does not reflect a true lack of solar wind control of these features.

[29] Our observation that the central cavity magnetic field enhancement correlates with β is consistent with earlier reports [Whang and Ness, 1972; Ogilvie and Ness, 1969] (though these authors also found a more clear correlation between the decrease in the expansion region and β than we see), as is our finding that the magnitude of the cavity enhancement does not change with solar wind magnetic field orientation [Colburn *et al.*, 1971].

[30] Less clear evidence of solar wind control is seen in the electrostatic potential data. The potential drop is slightly greater for higher solar wind magnetic fields, and is slightly deeper and wider when solar wind magnetic field and velocity are parallel, in both quasi-parallel and quasi-perpendicular regions of the wake, probably because particle access to the wake is more difficult when the solar wind magnetic field and velocity are close to parallel. The potential drop is clearly greater for higher solar wind velocity, probably because at the LP orbit, solar wind plasma has had less time to fill in the wake. The potential drop is also slightly wider for higher proton temperature. Little evidence for solar wind control is seen for other parameters.

3.3. Wave Velocity and Anisotropy

[31] Several previous authors have discussed whether it is appropriate to characterize the lunar wake in terms of ion sonic or magnetosonic processes. On the basis of measurements from Wind and the results of a simple one-dimensional simulation, Farrell *et al.* [1998] argued that ion sonic processes primarily determine the structure of the wake, and that the role of magnetic field orientation is of secondary importance, with magnetic field lines frozen into the plasma and responding to its movements. Clack *et al.* [2004], on the

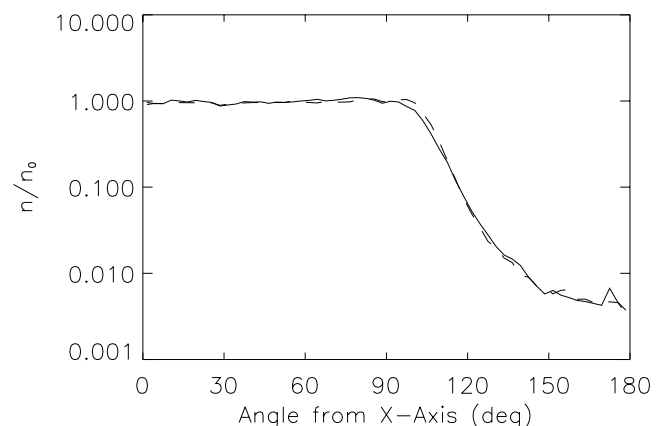


Figure 11. Normalized LP electron density measurements from orbital altitudes of 20–115 km, binned by angle from the wake axis, within 45° of the x - z plane (solid line) and within 45° of the x - y plane (dashed line).

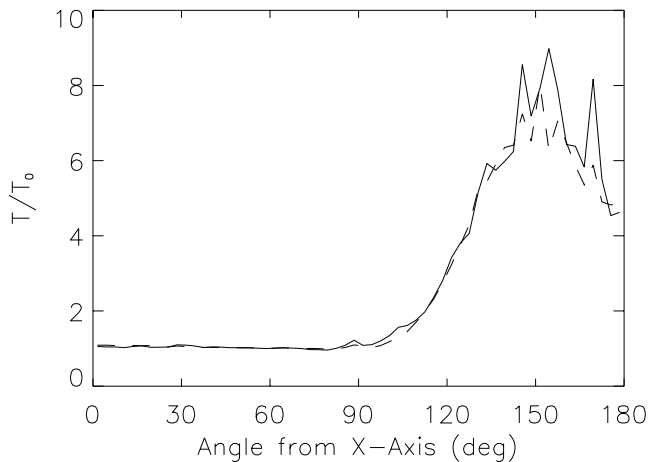


Figure 12. Normalized LP electron temperature measurements from orbital altitudes of 20–115 km, binned by angle from the wake axis, within 45° of the x - z plane (solid line) and within 45° of the x - y plane (dashed line).

other hand, demonstrated that ions, at least, closely follow the magnetic field when filling in the wake. As these authors point out, because of the low plasma density and enhanced magnetic field in the central wake, the plasma β in the wake cavity is low, suggesting that a magnetosonic characterization of the interaction may be more correct. In any case, ion dynamics may not convey the whole picture, as the simulations of *Birch and Chapman* [2001] suggest that electron dynamics dominate the evolution of the wake. Two main measurements are particularly crucial in determining what physical processes are most important: the speed at which plasma fills in the wake, and the velocity anisotropy with respect to the magnetic field direction.

[32] We attempt to address the first question by investigating the evolution of the wake as a function of convection time past the limb and distance from the wake boundary. We bin magnetic field data as a function of these two variables in a region near the lunar limb, and show the result in Figure 16. We choose to use magnetic field data because of the magnetic signatures clearly associated with each region of plasma compression and rarefaction. We see a slight enhancement, on average, in the magnetic field near the limb, associated with the transient limb shocks, though a high degree of variability is present in this region because of the influence of surface crustal fields, especially at low altitudes. Meanwhile, the magnetic field depression in the expansion region is clearly seen behind this enhancement. The enhanced fields in the central wake are not shown in this plot, since the magnetic field increase from the minimum in the expansion region is the only feature necessary for our purposes here.

[33] As *Schubert and Lichtenstein* [1974] have very cogently argued, it is difficult to define a Mach cone with respect to the undisturbed solar wind because of the presence of the limb shocks. The only true Mach cone with respect to the undisturbed solar wind must lie outside of these compressional features. We wish to focus on the steady state wake structure, rather than these transient features, and so can only look, in general, at local Mach surfaces (in practice, our data coverage is insufficient to

investigate the outermost Mach surface, in any case). We could in principle look at the rarefaction wave traveling outward from the limb (outer edge defined by the outside edge of the region of reduced fields) or the recompression wave traveling inward (outer edge defined by the minimum of the region of reduced fields). Unfortunately, our data coverage is such that the outer edge of the rarefaction wave is not well defined by our measurements. However, the surface defined by the outer edge of the recompression wave is well defined, and we have marked its approximate position with a dashed line in Figure 16. We find that the average speed of the recompression wave so defined is ~ 75 km/s. This is significantly higher than the average solar wind sound speed of ~ 44 km/s derived from the solar wind electron temperatures measured by LP. The local sound speed is somewhat higher because of the slight increase in electron temperature as you move into the wake (in the central wake, of course, the local sound speed will be much larger because of the huge increase in electron temperature), but probably not enough to explain this discrepancy. The recompression wave may instead travel at magnetosonic speeds, which, averaging over propagation angles, should lie between the average solar wind Alfvén speed of ~ 53 km/s and the average solar wind fast magnetosonic speed of ~ 69 km/s ($V_{MS} = \sqrt{V_A^2 + C_S^2}$). Even this speed is somewhat too small, but given that both the Alfvén speed and the sound speed should increase in the wake (because of the decrease in plasma density and the increase in electron temperature), the local magnetosonic speed will increase, and this discrepancy is therefore not inconsistent with expectations.

[34] We can attack this problem in another way by looking at the anisotropy of the plasma infilling with respect to magnetic field orientation. To address this anisotropy, we use the electron density. The magnetic field data are unsuitable, because the magnetic field manifestation of the rarefaction wave that we have previously used to track wave speed is naturally asymmetric with respect to the magnetic field, because of the previously discussed asymmetry in diamagnetic current systems. We choose the density over

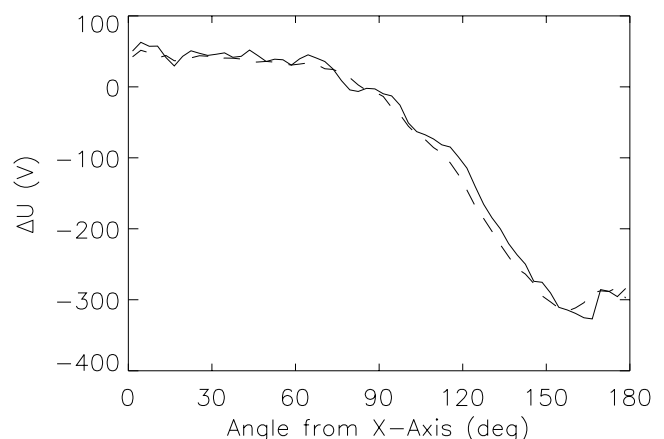


Figure 13. LP electrostatic potential measurements from orbital altitudes of 20–115 km, binned by angle from the wake axis, within 45° of the x - z plane (solid line) and within 45° of the x - y plane (dashed line).

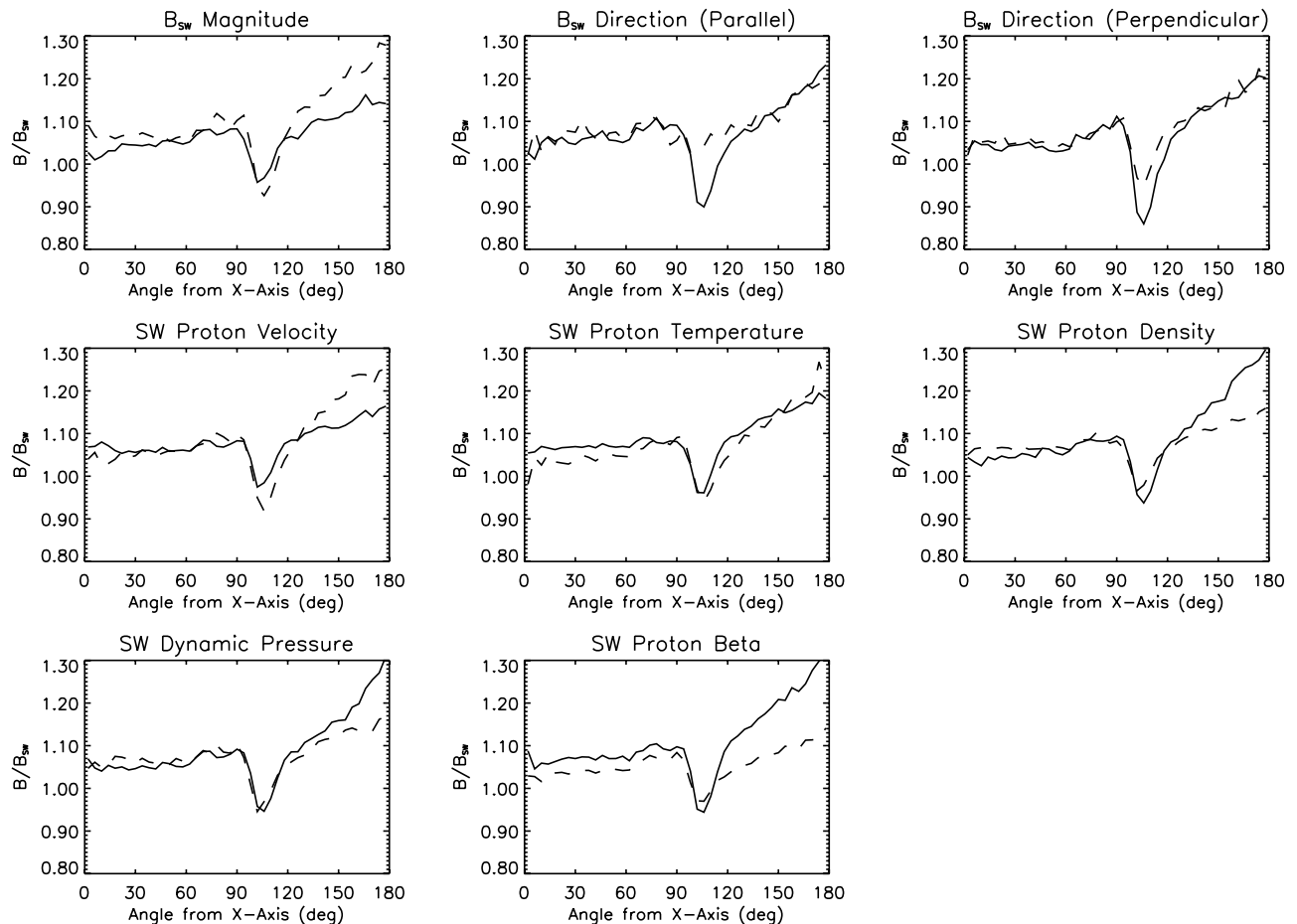


Figure 14. Normalized LP magnetic field measurements from altitudes of 85–115 km for the following (row by row, from left to right): solar wind magnetic fields >7.5 nT (solid line) and <5 nT (dashed line) (first panel); solar wind magnetic field angles within 25° of the solar wind velocity (solid line) and within 25° of perpendicular to the solar wind velocity (dashed line) for measurements within 45° of the x - z plane (second panel); solar wind magnetic field angles within 25° of the solar wind velocity (solid line) and within 25° of perpendicular to the solar wind velocity (dashed line) for measurements within 45° of the x - y plane (third panel); solar wind proton velocities >425 km/s (solid line) and <375 km/s (dashed line) (fourth panel); solar wind proton temperatures >8 eV (solid line) and <4 eV (dashed line) (fifth panel); solar wind proton densities >8 cm^{-3} (solid line) and <5 cm^{-3} (dashed line) (sixth panel); solar wind dynamic pressures >2 nPa (solid line) and <1.2 nPa (dashed line) (seventh panel); and solar wind proton $\beta > 0.5$ (solid line) and <0.25 (dashed line) (eighth panel).

other electron parameters because it changes the most rapidly on entrance to the wake.

[35] To ensure the maximum likelihood of finding an asymmetry in the way plasma fills in the wake, we apply a number of filters to the data. To guarantee the greatest asymmetry, we choose only data from times when the solar wind magnetic field is within 25° of perpendicular to the wake axis, and only those times when the field is relatively steady in orientation. We then select data from narrow regions around the wake x - z plane (nearly parallel to the magnetic field) and around the wake x - y plane (nearly perpendicular to the magnetic field). The resulting data are shown binned by angle from the wake axis in Figure 17. We find that any discernible asymmetry is below the level of the noise in the data. To the accuracy of our data, therefore, the plasma fills in the wake in a manner that is rotationally symmetric about the axis, and not strongly

controlled by magnetic field orientation. However, since the LP orbit lies so close to the Moon, any small rotational asymmetry about the wake axis will be difficult to detect, and the lack of any observed asymmetry should not be too surprising.

[36] It is instructive to compare our data to several representative cases. First of all, a completely sonic expansion, where the magnetic field is frozen into the plasma and dragged along as the plasma moves, would result in complete rotational symmetry about the wake axis. On the other hand, if the magnetic field remains completely fixed and plasma moves along the field lines, the profiles shown in Figure 18 would result (here we assume that plasma always expands along magnetic field lines as it does along the axis parallel to magnetic field in Figure 17, and calculate the resulting profile perpendicular to the magnetic field). This case is clearly not

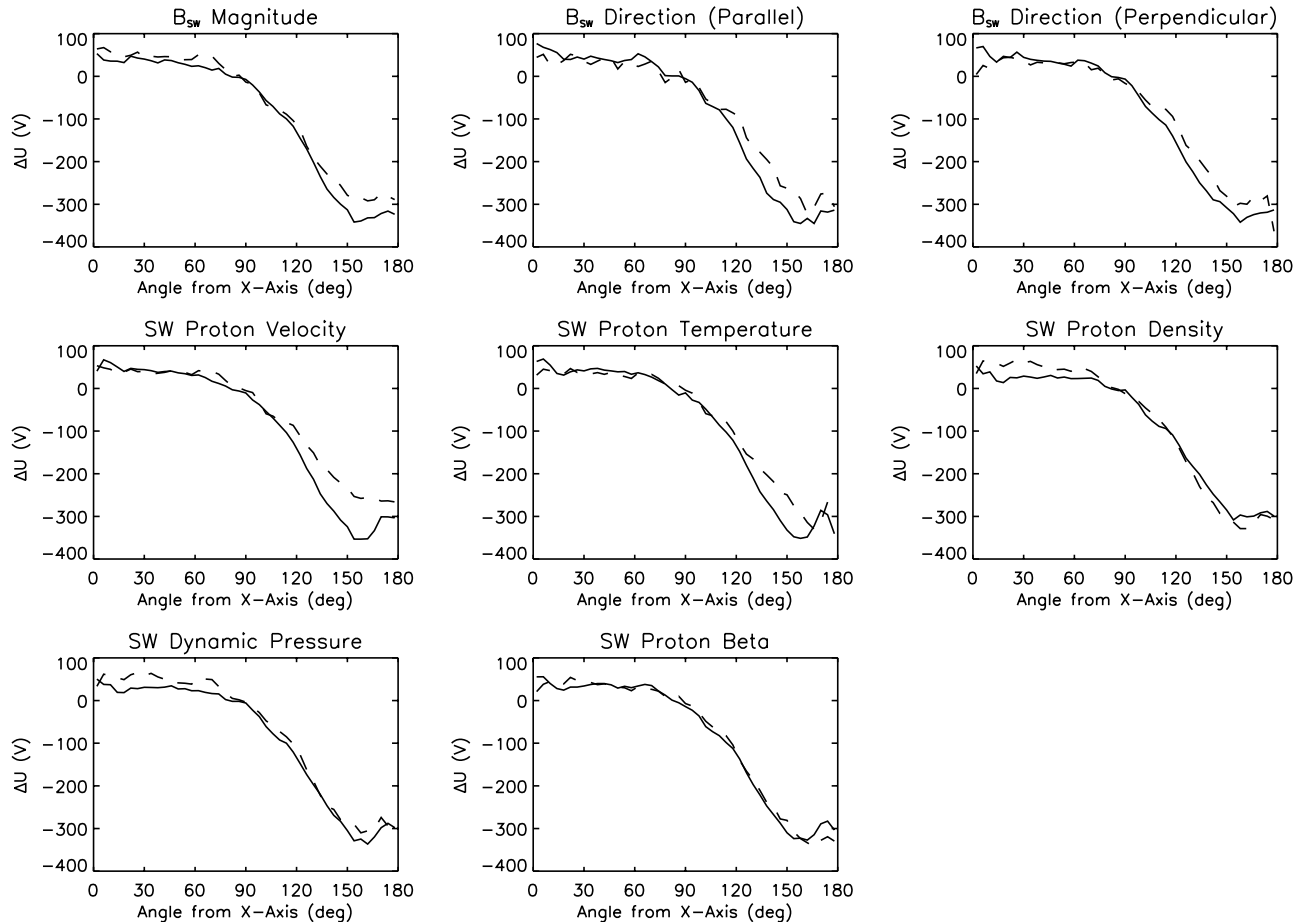


Figure 15. LP electrostatic potential measurements from altitudes of 20–115 km for the following (row by row, from left to right): solar wind magnetic fields >7.5 nT (solid line) and <5 nT (dashed line) (first panel); solar wind magnetic field angles within 25° of the solar wind velocity (solid line) and within 25° of perpendicular to the solar wind velocity (dashed line) for measurements within 45° of the x - z plane (second panel); solar wind magnetic field angles within 25° of the solar wind velocity (solid line) and within 25° of perpendicular to the solar wind velocity (dashed line) for measurements within 45° of the x - y plane (third panel); solar wind proton velocities >425 km/s (solid line) and <375 km/s (dashed line) (fourth panel); solar wind proton temperatures >8 eV (solid line) and <4 eV (dashed line) (fifth panel); solar wind proton densities >8 cm^{-3} (solid line) and <5 cm^{-3} (dashed line) (sixth panel); solar wind dynamic pressures >2 nPa (solid line) and <1.2 nPa (dashed line) (seventh panel); and solar wind proton $\beta > 0.5$ (solid line) and <0.25 (dashed line) (eighth panel).

consistent with our data. Finally, we calculate the same profiles assuming infilling via a fast magnetosonic plasma wave, with a velocity anisotropy of 1.3 (corresponding to the average solar wind Alfvén and sound speeds shown in Table 1, and isotropic plasma temperatures), and show the results in Figure 19. This case is virtually indistinguishable from our data. We conclude that our data lie too near the Moon to distinguish between sonic or magnetosonic expansion, unless the average magnetoacoustic velocity anisotropy greatly exceeds 1.3. The data of Clack *et al.* [2004] show that ions do in fact have high temperature anisotropies inside the wake, which could lead to higher magnetoacoustic velocity anisotropies; however, near the boundary of the wake these temperature anisotropies are not as large, and should not lead to much higher velocity anisotropies. Furthermore, though we have not systematically calculated temperature anisot-

ropies for the electrons, for every case we have investigated in detail, electron temperature anisotropies are relatively small even in the central wake.

[37] Two previous studies have addressed the magnetoacoustic velocity anisotropy [Whang and Ness, 1970; Sonett and Mihalov, 1972]. However, both of these studies relied on magnetic field data, which are naturally asymmetric with respect to the magnetic field orientation, and they looked at two different local Mach surfaces, making comparison with our results difficult. Nonetheless, Whang and Ness [1970], who looked at the outer edge of the rarefaction wave, derived a magnetoacoustic velocity anisotropy of 1.4, consistent both with our results and typical solar wind parameters. Sonett and Mihalov [1972], on the other hand, looked at the peaks of the limb shocks, and derived a much higher velocity anisotropy of 3, inconsistent with our results and with typical solar wind parameters.

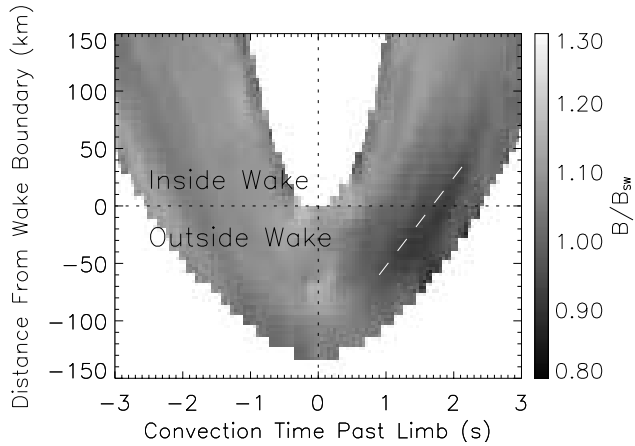


Figure 16. Normalized LP magnetic field measurements, binned by convection time past the limb and distance from the wake boundary (defined as a cylinder with the radius of the Moon and aligned with the wake axis). Dashed line shows approximate outer edge of recompression wave. Dotted lines show limb and wake boundary. See color version of this figure at back of this issue.

[38] Another question that these previous studies attempted to address was whether the local Mach surfaces begin right at the lunar surface or are instead “detached.” The data presented in Figure 16 conclusively show that though limb shocks and rarefaction/recompression waves may begin up to ~ 50 km above the surface, they are not detached to the degree suggested by *Sonett and Mihalov* [1972], who inferred a Mach cone detached from the surface by hundreds of km.

4. Simple Theory and Interpretation

[39] The refilling of the lunar wake cavity by solar wind plasma is essentially a case of plasma expansion into a vacuum, which a number of authors have addressed [e.g., *Crow et al.*, 1975; *Denavit*, 1979; *Singh and Schunk*, 1982; *Samir et al.*, 1983]. Of course, the lunar case is made more

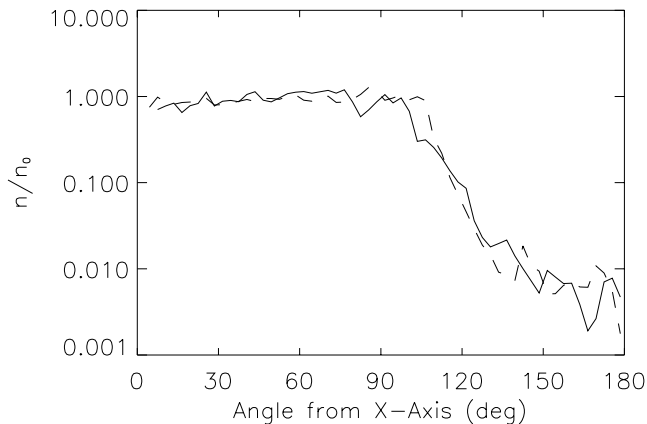


Figure 17. Normalized LP electron density measurements for orbits with very steady solar wind magnetic fields, binned by angle from the wake axis, within 15° of the x - z plane (solid line) and within 15° of the x - y plane (dashed line) for solar wind magnetic field angles within 25° of perpendicular to the solar wind velocity.

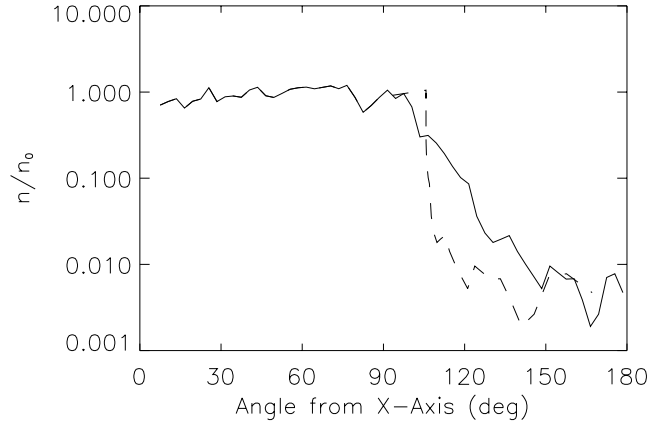


Figure 18. Solid line as for Figure 17. Dashed line shows a density profile corresponding to that in Figure 17 but assuming no deformation of field lines and particle motion only along field lines.

complex by, among other things, plasma flow, the presence of the Moon and its crustal magnetic fields, and the possibility of plasma instabilities, but we may nonetheless gain valuable insights from the results derived for initially stationary unmagnetized plasmas. For the case of a single ion species (protons), it is not too difficult to derive simple 1-D self-similar equations for the expansion (as a function of distance from the initial plasma-void boundary s and expansion time t), by starting with the ion continuity and momentum equations (equations (1)–(2)), and the Boltzmann relation (equation (3), assuming isothermal expansion, and using energy units for electron temperature).

$$\frac{\partial N_i}{\partial t} + \frac{\partial}{\partial s}(N_i V_i) = 0 \quad (1)$$

$$\frac{\partial V_i}{\partial t} + V_i \frac{\partial V_i}{\partial s} + \frac{e}{M_i} \frac{\partial \phi}{\partial s} = 0 \quad (2)$$

$$N_e = N_0 \exp(e\phi/T_e) \quad (3)$$

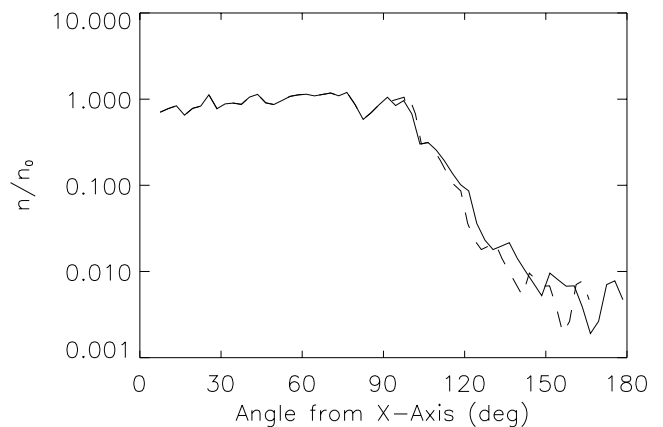


Figure 19. Solid line as for Figure 17. Dashed line shows a density profile corresponding to that in Figure 17 but assuming fast magnetosonic expansion with a magnetoacoustic velocity anisotropy of 1.3.

[40] Assuming quasi-neutrality ($N_e = N_i$) one can easily solve these coupled equations to derive the following self-similar solutions, which depend only on $Z = s/t$ and the speed of sound $C_s = \sqrt{T_e/M_i}$.

$$N_e = N_0 \exp(-(Z/C_s + 1)) \quad (4)$$

$$\varphi = -(T_e/e)(Z/C_s + 1) \quad (5)$$

$$V_i = Z + C_s \quad (6)$$

[41] These isothermal expansion solutions, which essentially summarize results from *Samir et al.* [1983], show that the electron density decreases exponentially into the void, a potential drop is set up between the plasma and the void, and ions are accelerated into the void region. Several authors have shown via computer simulations and theoretical calculations that, even with the assumption of quasi-neutrality removed, self-similar solutions remain approximately correct except at the far edge of the expansion (i.e., high Z), where a pure electron cloud precedes an “ion front” [*Crow et al.*, 1975; *Denavit*, 1979; *Singh and Schunk*, 1982]. When one introduces other complexities, such as the existence of multiple species of ions, solutions also naturally become more complicated. In general, however, the expansion remains qualitatively similar.

[42] One major drawback of the formalism presented above is the assumption of isothermal expansion, which allows the use of the Boltzmann relation for the electrons. For a Maxwellian distribution this assumption is valid, because when one filters a Maxwellian distribution through a potential drop, the kinetic temperature remains the same. However, as discussed previously, this is not true for electron distributions like those observed in the solar wind, which instead have high-energy tails more aptly described by Kappa functions. When Kappa functions are used to describe the particle distribution functions, the following relations, analogous to the Boltzmann relation (equation (3)), can instead be derived.

$$T_e = T_0 \left[1 - \frac{1}{(\kappa - 3/2)} \frac{e\varphi}{T_0} \right] \quad (7)$$

$$N_e = N_0 \left[1 - \frac{1}{(\kappa - 3/2)} \frac{e\varphi}{T_0} \right]^{(1/2-\kappa)} \quad (8)$$

[43] By using these new relations, along with the same ion momentum and continuity equations, we can proceed in an analogous manner to derive a completely new set of self-similar equations for plasma expansion into a void, assuming Kappa function distributions.

$$N_e = N_0 \left[1 + \frac{1}{(2\kappa - 2)} \sqrt{\frac{2\kappa - 1}{2\kappa - 3}} (Z/C_s + 1) \right]^{(1-2\kappa)} \quad (9)$$

$$T_e = T_0 \left[1 + \frac{1}{(2\kappa - 2)} \sqrt{\frac{2\kappa - 1}{2\kappa - 3}} (Z/C_s + 1) \right]^2 \quad (10)$$

$$\varphi = -(T_0/e)(\kappa - 3/2) \left\{ \left[1 + \frac{1}{(2\kappa - 2)} \sqrt{\frac{2\kappa - 1}{2\kappa - 3}} (Z/C_s + 1) \right]^2 - 1 \right\} \quad (11)$$

$$V_i = Z + \frac{1}{(2\kappa - 2)} (Z + C_s) + \sqrt{\frac{2\kappa - 3}{2\kappa - 1}} C_s \quad (12)$$

[44] One can verify that these new Kappa function solutions reduce to previously derived isothermal solutions for $\kappa \rightarrow \infty$, thus recovering Maxwellian distributions. For small kappa parameters, however, these new solutions differ significantly from isothermal solutions, especially for the electron temperature (which instead of remaining constant, increases substantially with Z , as expected). It is important to note that these solutions are only valid for $Z > -C_s$ (the outside edge of the rarefaction wave, beyond which the plasma remains undisturbed).

4.1. Electron Behavior

[45] Naturally, we wish to apply this new formalism and see how well it fits our data. To this end, we show binned data for all orbital altitudes and solar wind parameters in Figures 20–22 as a function of the variable Z , along with theoretical curves using the forms derived in equations (9)–(11), for a variety of different kappa parameters. There is a fair amount of scatter, but the data do cluster to some degree when plotted against the variable Z (especially the normalized electron density and electrostatic potential data), supporting the use of self-similar solutions. None of the solutions are completely adequate to describe the normalized electron density data, but the Kappa function solutions are clearly better than the Maxwellian solution, and fit the data fairly well for $Z < \sim 300$. As for the normalized electron temperature data and the electrostatic potential data, Kappa function solutions for kappa parameters between 3 and the average solar wind value of ~ 4.5 fit the data well, though again the fit is better for $Z < \sim 300$. Considering that our simple theory is completely one-dimensional and does not account for the presence of a magnetic field, we consider these fits rather good. The fits may worsen at high Z because quasi-neutrality is no longer valid at the outer edge of plasma expansion [*Crow et al.*, 1975; *Denavit*, 1979; *Singh and Schunk*, 1982], and/or because of the presence of plasma instabilities [*Farrell et al.*, 1998; *Birch and Chapman*, 2001]. Also, as expected, the solutions do not fit the data for $Z < -C_s$, as this is outside of their region of validity. In general, however, Kappa function solutions fit the data reasonably well, and much better than solutions for isothermal expansion (i.e., Maxwellian distributions).

4.2. Wave Velocity

[46] As a helpful reviewer pointed out, the newly derived equations for self-similar expansion introduce a new effective velocity (see equation (12)). One might expect that this could help explain the recompression wave velocity noted earlier. Indeed, the new velocity is slightly greater than that derived for an isothermal expansion; however, near the wake boundary the difference is minimal. It appears that

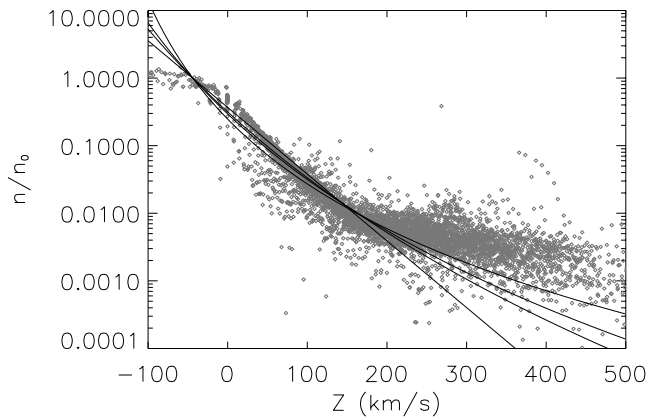


Figure 20. Normalized LP electron density measurements binned by convection time past the limb t and distance from the wake boundary s , as a function of $Z = s/t$ (light shaded diamonds), and theoretical curves for $\kappa = 3.0$ (most curved line), 4.5, 6.0, and infinity (straight line, equivalent to assuming a Maxwellian distribution).

our 1-D treatment is not capable of explaining the high recompression wave velocity. Instead, it seems likely that a full magnetosonic treatment that takes into account the 2-D or even 3-D character of the expansion would be required to fully explain this wave velocity.

4.3. Magnetic Field Behavior

[47] We can also use the Kappa function solutions for plasma expansion into a void derived above to calculate the expected magnetic field signature. The density and temperature solutions instantly give the electron pressure (and the gradient thereof), and we can then calculate diamagnetic currents for any solar wind magnetic field orientation. From the diamagnetic currents, we can use the Biot-Savart law to calculate the resulting magnetic field perturbations, using a Monte Carlo integration over the entire wake. We show the

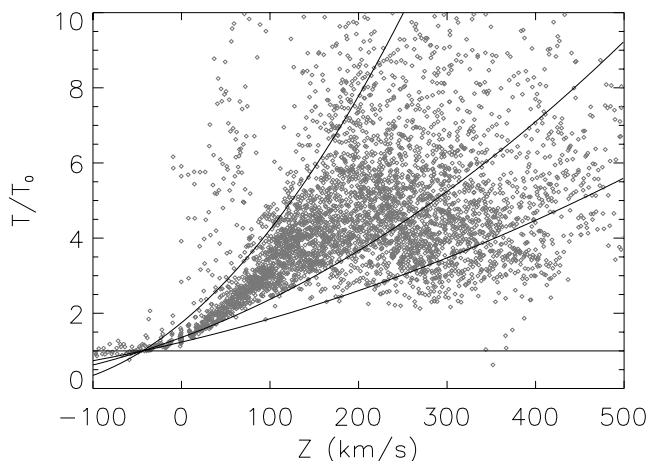


Figure 21. Normalized LP electron temperature measurements binned by convection time past the limb t and distance from the wake boundary s , as a function of $Z = s/t$ (light shaded diamonds), and theoretical curves for $\kappa = 3.0$ (most curved line), 4.5, 6.0, and infinity (straight line, equivalent to assuming a Maxwellian distribution).

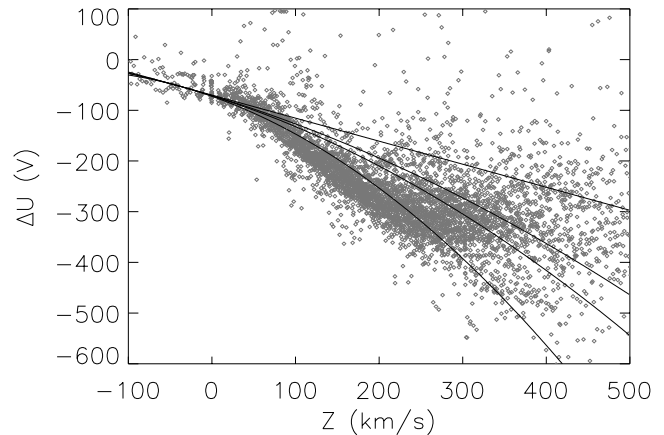


Figure 22. LP electrostatic potential measurements binned by convection time past the limb t and distance from the wake boundary s , as a function of $Z = s/t$ (light shaded diamonds), and theoretical curves for $\kappa = 3.0$ (most curved line), 4.5, 6.0, and infinity (straight line, equivalent to assuming a Maxwellian distribution).

results of this simple exercise in Figures 23–24 in terms of normalized magnetic field versus angle from the wake axis, in the wake x - z plane (parallel to the magnetic field direction) and in the wake x - y plane (perpendicular to the magnetic field direction), each for solar wind magnetic fields parallel and perpendicular to the wake axis. These plots can be directly compared to the second and third panels of Figure 14. The models are qualitatively and quantitatively similar to the data, showing reduced magnetic fields in the expansion region and enhanced fields in the central wake, with the size of the magnetic perturbations roughly correct. As we observe for our data, model fields are not reduced in the expansion region of the wake x - z plane when the unperturbed magnetic field is perpendicular to the wake axis, because the pressure gradient is parallel to the magnetic field there and produces no diamagnetic currents.

[48] There are, however, a number of discrepancies between the model fields and our data. First, for obvious reasons, there are no limb shocks forward of the expansion region in the model, since we do not include any lunar crustal fields. The degree to which the resulting profiles differ does give us a good idea of how important the limb shocks are in determining the magnetic field morphology in the region forward of the expansion region, on average (naturally, for those times when strong limb shocks are present, the effect is still more pronounced). The other major discrepancy between the model fields and our data lies in the central wake. Our models predict a magnetic enhancement that increases rapidly just inside the expansion region, producing a wide region of increased magnetic fields. Our data, in contrast, show a magnetic enhancement that increases much more gradually and only peaks near the wake axis. Furthermore, our models predict a much larger enhancement when the solar wind magnetic field is parallel to the wake axis. This is presumably because diamagnetic currents are present around the entire wake surface in this case, rather than just on two sides, which should lead to a larger enhancement in the central wake (this agrees with

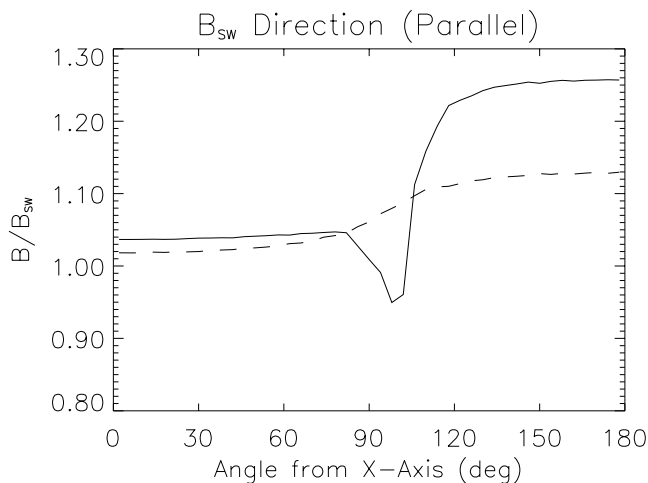


Figure 23. Model magnetic field perturbation as a function of angle from the wake axis for solar wind magnetic field parallel to the solar wind velocity (solid line) and perpendicular to the solar wind velocity (dashed line) in the x - z plane.

previous model and theoretical results [Ness *et al.*, 1968; Whang, 1968b]). However, our data show no such effect. Inductive currents in the Moon or a time delay in the magnetic response to the wake formation may help explain the more gradual increase in magnetic field in the central wake seen in our data. However, we have no explanation for the discrepancy in the magnitude of the enhancement for parallel and perpendicular cases. We can only speculate that this effect may be due to differences in the pressure gradients in the two cases, or the presence of significant pressure anisotropies. Alternatively, the discrepancy could be produced by differences in the closure currents (for the parallel case currents close around the wake, while for the perpendicular case currents close around and/or through the Moon and far down the wake).

4.4. Overview

[49] In general, simple Kappa function solutions for plasma expansion into a void reproduce the gross features of the lunar wake in terms of both electron parameters and magnetic field perturbations. Though these models are not completely successful in reproducing all the features of the data, they describe most of the basic morphology of the wake. More complicated 2-D or 3-D models incorporating, for instance, the conductive lunar surface, lunar crustal magnetic fields, pressure/temperature anisotropies, etc. should be capable of doing a better job, but such a significant modeling project is beyond the scope of this paper.

5. Conclusions

[50] Our data describe a lunar wake controlled by an interesting mix of kinetic and fluid plasma physics. As the solar wind flows past the Moon, solar wind plasma is absorbed and neutralized, creating a cavity behind the Moon. Plasma begins to expand into the resulting void as it flows past the lunar limb, with faster electrons leading

ions into the wake. This mismatched expansion produces a charge separation, setting up a potential difference between the solar wind and the central wake, and thereby slowing the electrons and accelerating the ions. The physics of the expansion is significantly altered by the non-Maxwellian nature of the solar wind electrons, leading to greatly enhanced electron temperatures in the wake, and a larger potential drop and a less steep falloff in electron density than would be predicted for an isothermal expansion. Meanwhile, the gradient in pressure across the wake boundary creates diamagnetic currents that in turn produce significant magnetic field perturbations in and around the wake. The morphology of the magnetic perturbations depends strongly on the solar wind magnetic field orientation with respect to the wake axis. However, at lower altitudes, regardless of solar wind magnetic field orientation, the effects of lunar crustal fields dominate over these wake-related perturbations.

[51] The lunar wake clearly responds to changes in the ambient solar wind, with the response especially clearly expressed in terms of magnetic field morphology, with particularly significant changes resulting from differences in solar wind magnetic field magnitude and direction, and proton velocity, density, and β . Possibly because of the limitations of our data, the electron response is not seen as clearly as that for magnetic fields, though we do observe some slight changes in response to differing solar wind magnetic fields and proton velocity and temperature.

[52] We observe a wake that refills, to the limits of what our data can resolve, in a manner approximately rotationally symmetric about the wake axis. However, our data are roughly consistent with either a completely sonic expansion or a magnetosonic expansion with a small magnetoacoustic velocity anisotropy. The velocity of the recompression wave is more consistent with magnetosonic than sonic velocities, but neither can be completely ruled out.

[53] The basic morphology of the wake, in terms of both electron parameters and magnetic fields, is well reproduced

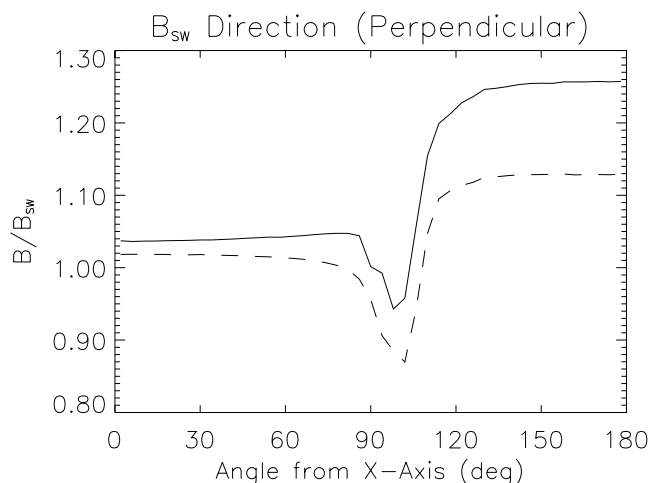


Figure 24. Model magnetic field perturbation as a function of angle from the wake axis for solar wind magnetic field parallel to the solar wind velocity (solid line) and perpendicular to the solar wind velocity (dashed line) in the x - y plane.

by self-similar solutions for plasma expansion into a void, but only when the solutions are modified to use Kappa function electron distributions rather than assuming isothermal Maxwellian expansion.

[54] **Acknowledgments.** This work was supported by NASA award FDNN04GA94G-01/05. We thank two reviewers for insightful and helpful comments that greatly strengthened this manuscript.

[55] Lou-Chuang Lee thanks Timothy Stubbs and another reviewer for their assistance in evaluating this paper.

References

- Birch, P. C., and S. C. Chapman (2001), Detailed structure and dynamics in particle-in-cell simulations of the lunar wake, *Phys. Plasmas*, **8**, 4551–4559.
- Borisov, N., and U. Mall (2000), Plasma distribution and electric fields behind the Moon, *Phys. Lett. A*, **265**, 369–376.
- Borisov, N., and U. Mall (2002), The structure of the double layer behind the Moon, *J. Plasma Phys.*, **67**, 277–299.
- Bosqued, J. M., et al. (1996), Moon-solar wind interaction: First results from the Wind/3DP experiment, *Geophys. Res. Lett.*, **23**, 1259–1262.
- Clack, D., J. C. Kasper, A. J. Lazarus, J. T. Steinberg, and W. M. Farrell (2004), Wind observations of extreme ion temperature anisotropies in the lunar wake, *Geophys. Res. Lett.*, **31**, L06812, doi:10.1029/2003GL018298.
- Colburn, D. S., R. G. Currie, J. D. Mihalov, and C. P. Sonett (1967), Diamagnetic solar-wind cavity discovered behind moon, *Science*, **158**, 1040–1042.
- Colburn, D. S., J. D. Mihalov, and C. P. Sonett (1971), Magnetic observations of the lunar cavity, *J. Geophys. Res.*, **76**, 2940–2957.
- Crow, J. E., P. L. Auer, and J. E. Allen (1975), The expansion of plasma into a vacuum, *J. Plasma Phys.*, **14**, 65–76.
- Denavit, J. (1979), Collisionless plasma expansion into a vacuum, *Phys. Fluids*, **22**, 1384–1392.
- Farrell, W. M., M. L. Kaiser, J. T. Steinberg, and S. D. Bale (1998), A simple simulation of a plasma void: Applications to Wind observations of the lunar wake, *J. Geophys. Res.*, **103**, 23,653–23,660.
- Futaana, Y., S. Machida, Y. Saito, A. Matsuoka, and H. Hayakawa (2001), Counterstreaming electrons in the near vicinity of the Moon observed by plasma instruments on board NOZOMI, *J. Geophys. Res.*, **106**, 18,729–18,740.
- Goldstein, B. E. (1974), Observations of electrons at the lunar surface, *J. Geophys. Res.*, **79**, 23–35.
- Halekas, J. S., D. L. Mitchell, R. P. Lin, S. Frey, L. L. Hood, M. H. Acuña, and A. B. Binder (2001), Mapping of crustal magnetic anomalies on the lunar near side by the Lunar Prospector electron reflectometer, *J. Geophys. Res.*, **106**, 27,841–27,852.
- Halekas, J. S., D. L. Mitchell, R. P. Lin, L. L. Hood, and M. H. Acuña (2002), Evidence for negative charging of the lunar surface in shadow, *Geophys. Res. Lett.*, **29**(10), 1435, doi:10.1029/2001GL014428.
- Halekas, J. S., R. P. Lin, and D. L. Mitchell (2003), Inferring the scale height of the lunar nightside double layer, *Geophys. Res. Lett.*, **30**(21), 2117, doi:10.1029/2003GL018421.
- Hollweg, J. V. (1970), Lunar conducting islands and formation of a lunar limb shock wave, *J. Geophys. Res.*, **75**, 1209–1216.
- Hood, L. L., A. Zakharian, J. Halekas, D. L. Mitchell, R. P. Lin, M. H. Acuña, and A. B. Binder (2001), Initial mapping and interpretation of lunar crustal magnetic anomalies using Lunar Prospector data, *J. Geophys. Res.*, **106**, 27,825–27,840.
- Johnson, F., and J. E. Midgeley (1968), Notes on the lunar magnetosphere, *J. Geophys. Res.*, **73**, 1523–1532.
- Lepping, R. P., et al. (1995), The Wind magnetic field investigation, *Space Sci. Rev.*, **71**, 207–229.
- Lin, R. P., D. L. Mitchell, D. W. Curtis, K. A. Anderson, C. W. Carlson, J. McFadden, M. H. Acuña, L. L. Hood, and A. Binder (1998), Lunar surface magnetic fields and their interaction with the solar wind: Results from Lunar Prospector, *Science*, **281**, 1480–1484.
- Michel, F. C. (1968), Magnetic field structure behind the Moon, *J. Geophys. Res.*, **73**, 1533–1541.
- Nakagawa, T., Y. Takahashi, and M. Iizima (2003), Geotail observation of upstream ULF waves associated with the lunar wake, *Earth Planets Space*, **55**, 569–580.
- Ness, N. F. (1972), Interaction of the solar wind with the Moon, in *Solar Terrestrial Physics 1970*, part II, edited by E. R. Dyer, pp. 159–205, Springer, New York.
- Ness, N. F., K. W. Behannon, H. E. Taylor, and Y. C. Whang (1968), Perturbations of the interplanetary magnetic field by the lunar wake, *J. Geophys. Res.*, **73**, 3421–3440.
- Ogilvie, K. W., and N. F. Ness (1969), Dependence of the lunar wake on solar wind plasma characteristics, *J. Geophys. Res.*, **74**, 4123–4128.
- Ogilvie, K. W., et al. (1995), SWE, a comprehensive plasma instrument for the Wind spacecraft, *Space Sci. Rev.*, **71**, 55–77.
- Ogilvie, K. W., J. T. Steinberg, R. J. Fitzenreiter, C. J. Owen, A. J. Lazarus, W. M. Farrell, and R. B. Torbert (1996), Observations of the lunar plasma wake from the Wind spacecraft on December 27, 1994, *Geophys. Res. Lett.*, **23**, 1255–1258.
- Owen, C. J., R. P. Lepping, K. W. Ogilvie, J. A. Slavin, W. M. Farrell, and J. B. Byrnes (1996), The lunar wake at 6.8 R_L : Wind magnetic field observations, *Geophys. Res. Lett.*, **23**, 1263–1266.
- Russell, C. T., and B. R. Lichtenstein (1975), On the source of lunar limb compression, *J. Geophys. Res.*, **80**, 4700–4711.
- Samir, U., K. H. Wright Jr., and N. H. Stone (1983), The expansion of a plasma into a vacuum: Basic phenomena and processes and applications to space plasma physics, *Rev. Geophys.*, **21**, 1631–1646.
- Schubert, G., and B. R. Lichtenstein (1974), Observations of Moon-plasma interactions by orbital and surface experiments, *Rev. Geophys.*, **12**, 592–626.
- Scudder, J. D. (1992), Why all stars should possess circumstellar temperature inversions, *Astron. J.*, **398**, 319–349.
- Singh, N., and R. W. Schunk (1982), Numerical calculations relevant to the initial expansion of the polar wind, *J. Geophys. Res.*, **87**, 9154–9170.
- Siscoe, G. L., and N. R. Mukherjee (1972), Upper limits on the lunar atmosphere determined from solar wind measurements, *J. Geophys. Res.*, **77**, 6042–6051.
- Siscoe, G. L., E. F. Lyon, J. H. Binsach, and H. S. Bridge (1969), Experimental evidence for a detached lunar compression wave, *J. Geophys. Res.*, **74**, 59–69.
- Sonett, C. P. (1982), Electromagnetic induction in the Moon, *Rev. Geophys.*, **20**, 411–455.
- Sonett, C. P., and J. D. Mihalov (1972), Lunar fossil magnetism and perturbations of the solar wind, *J. Geophys. Res.*, **77**, 588–603.
- Whang, Y. C. (1968a), Interaction of the magnetized solar wind with the Moon, *Phys. Fluids*, **11**, 969–975.
- Whang, Y. C. (1968b), Theoretical study of the magnetic field in the lunar wake, *Phys. Fluids*, **11**, 1713–1719.
- Whang, Y. C., and N. F. Ness (1970), Observations and interpretation of the lunar Mach cone, *J. Geophys. Res.*, **75**, 6002–6010.
- Whang, Y. C., and N. F. Ness (1972), Magnetic-field anomalies in the lunar wake, *J. Geophys. Res.*, **77**, 1109–1115.

S. D. Bale, J. S. Halekas, R. P. Lin, and D. L. Mitchell, Space Sciences Laboratory, University of California, Berkeley, CA 94720, USA. (jazzman@ssl.berkeley.edu)

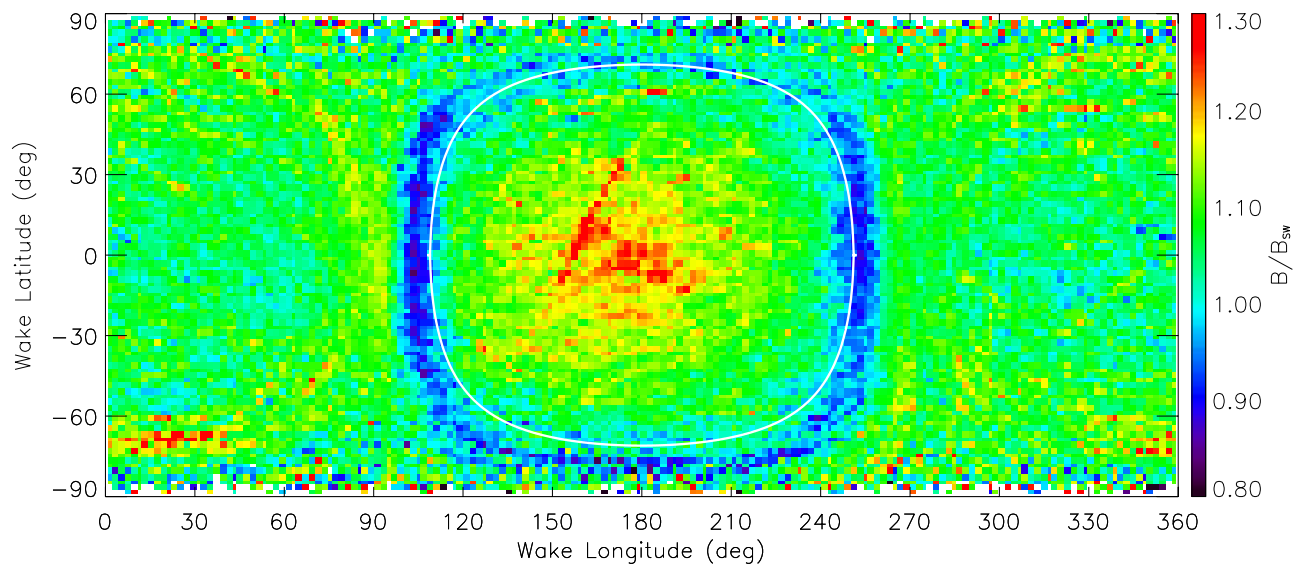


Figure 3. Normalized LP magnetic field measurements from altitudes of 85–115 km, binned by wake longitude and latitude. The white circle shows the solar wind flow terminator.

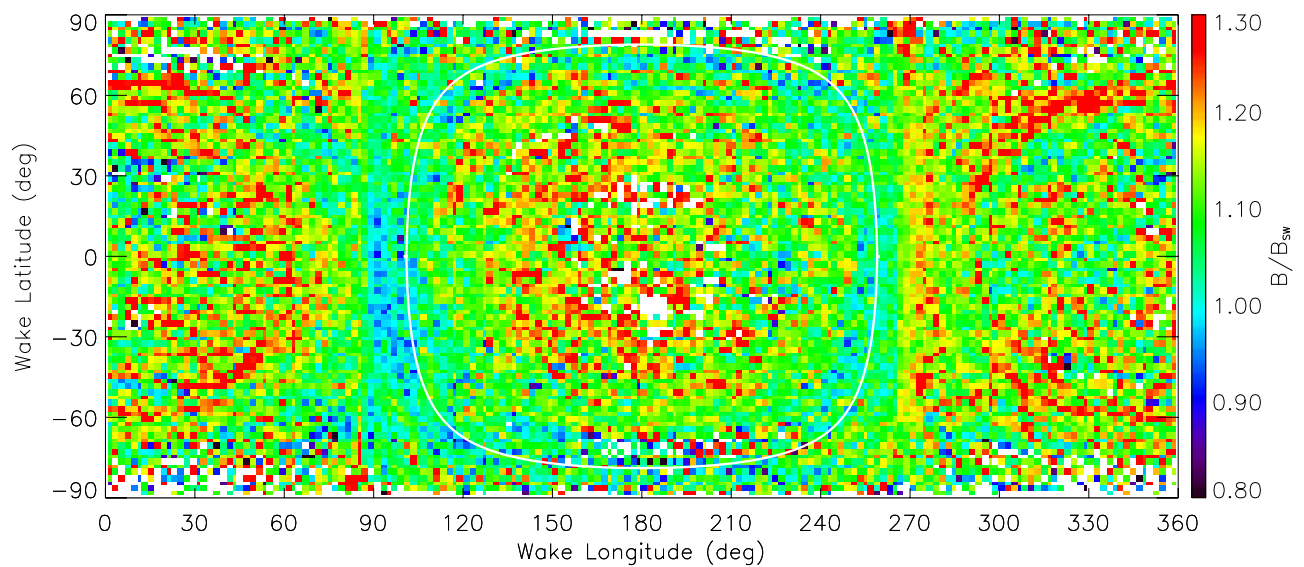


Figure 4. Normalized LP magnetic field measurements from altitudes of 20–45 km, binned by wake longitude and latitude. The white circle shows the solar wind flow terminator.

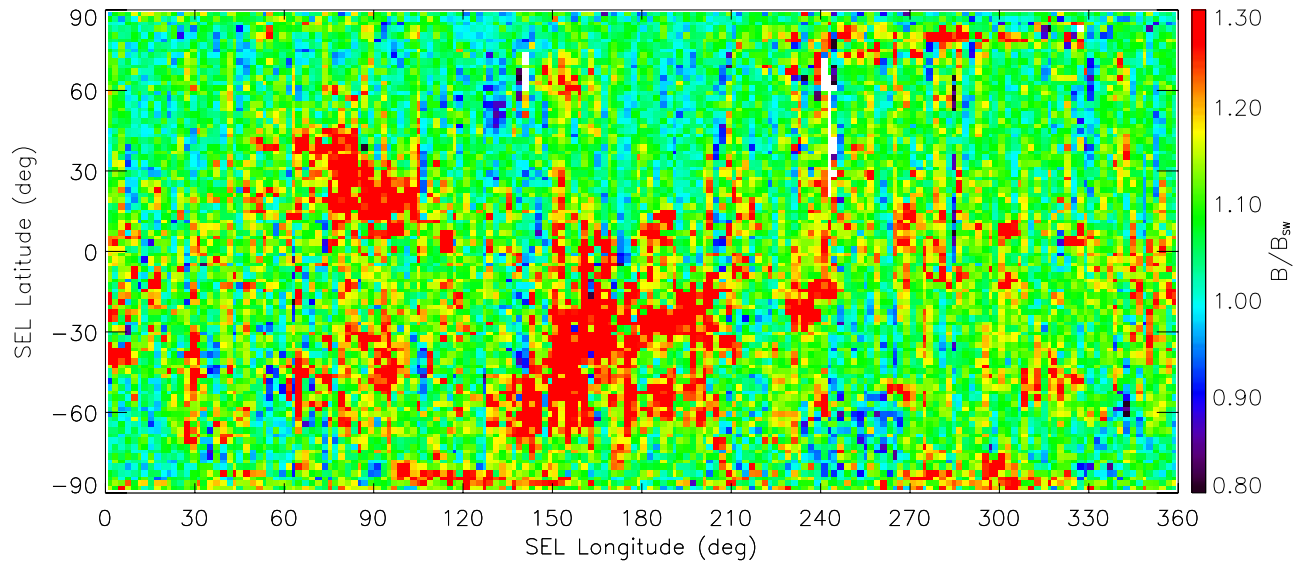


Figure 5. Normalized LP magnetic field measurements from altitudes of 20–45 km, binned by selenographic (SEL) longitude and latitude.

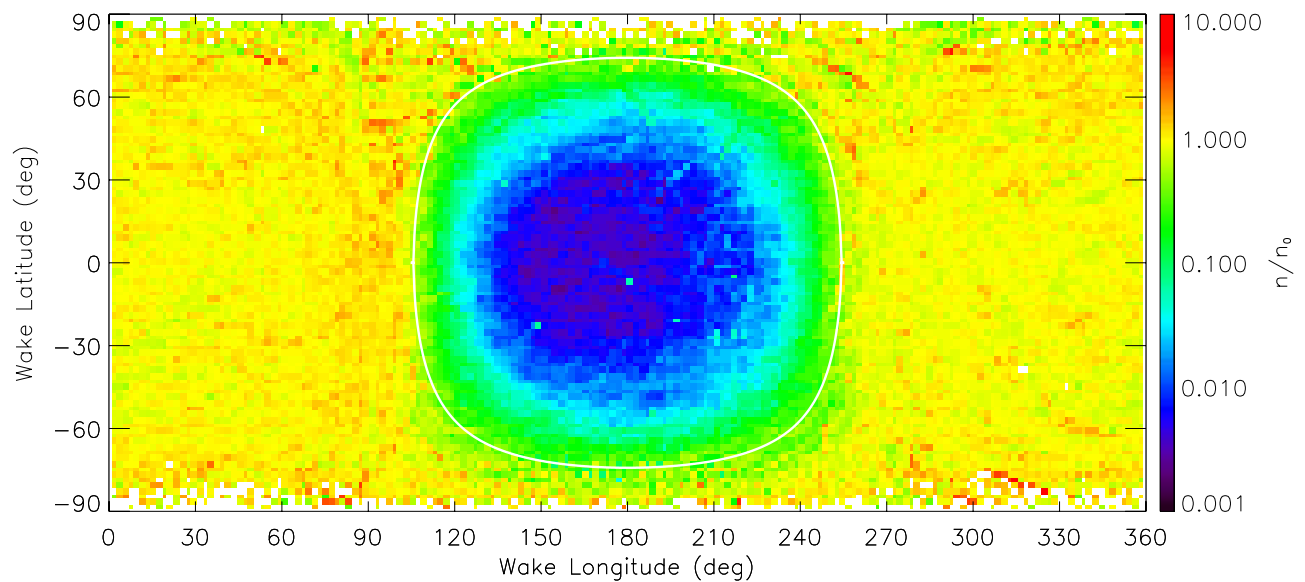


Figure 6. Normalized LP electron density measurements from altitudes of 20–115 km, binned by wake longitude and latitude. The white circle shows the solar wind flow terminator.

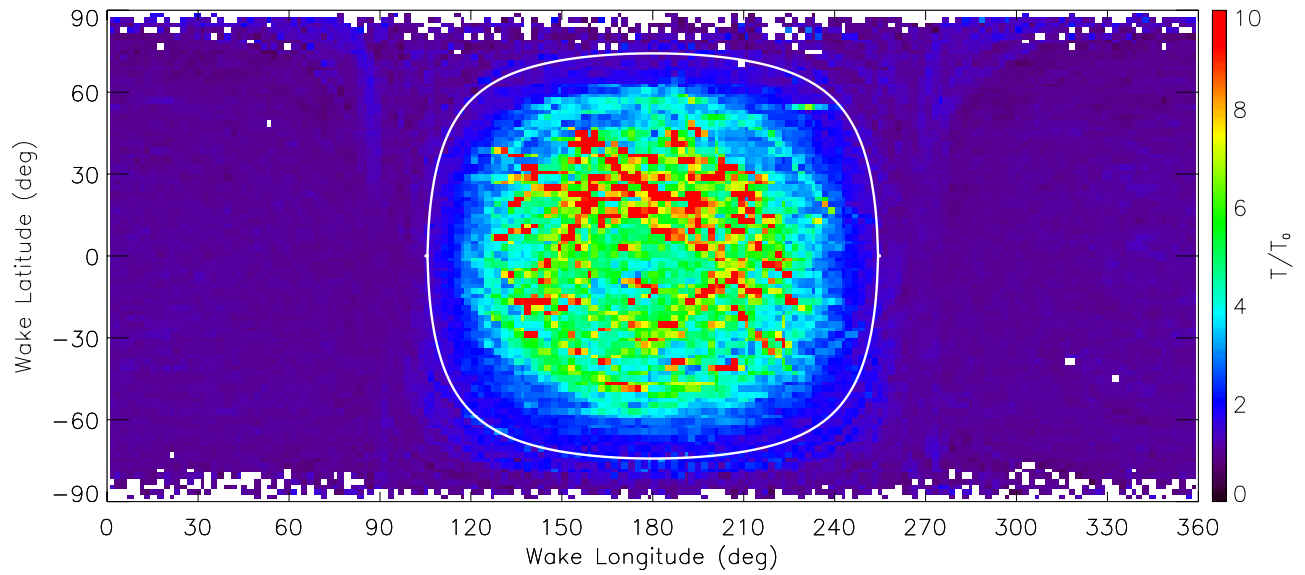


Figure 7. Normalized LP electron temperature measurements from altitudes of 20–115 km, binned by wake longitude and latitude. The white circle shows the solar wind flow terminator.

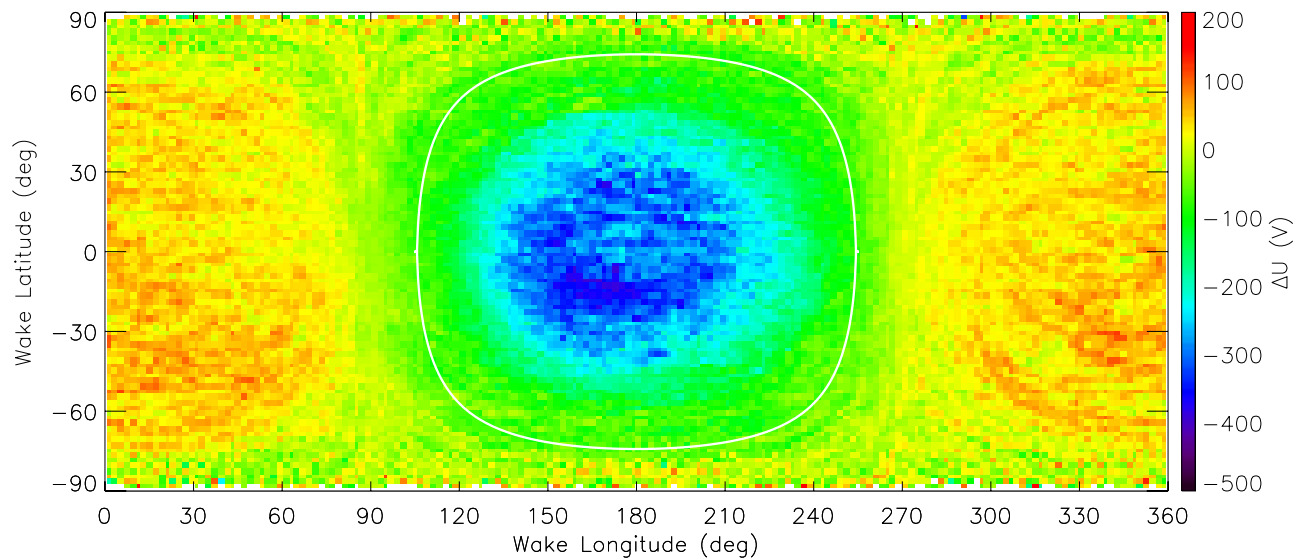


Figure 8. LP electrostatic potential measurements from altitudes of 20–115 km, binned by wake longitude and latitude. The white circle shows the solar wind flow terminator.

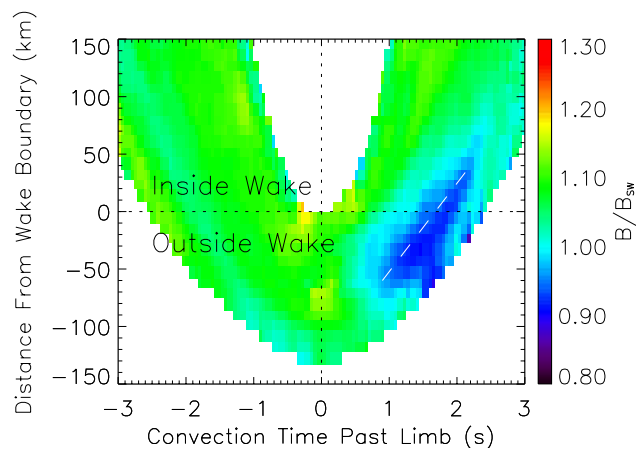


Figure 16. Normalized LP magnetic field measurements, binned by convection time past the limb and distance from the wake boundary (defined as a cylinder with the radius of the Moon and aligned with the wake axis). Dashed line shows approximate outer edge of recompression wave. Dotted lines show limb and wake boundary.